



# CHORUS

This is the accepted manuscript made available via CHORUS. The article has been published as:

## Stability of multiferroic phase and magnetization-polarization coupling in Y-type hexaferrite crystals

V. Kocsis, T. Nakajima, M. Matsuda, A. Kikkawa, Y. Kaneko, J. Takashima, K. Kakurai, T. Arima, Y. Tokunaga, Y. Tokura, and Y. Taguchi

Phys. Rev. B **101**, 075136 — Published 26 February 2020

DOI: [10.1103/PhysRevB.101.075136](https://doi.org/10.1103/PhysRevB.101.075136)

# Stability of multiferroic phase and magnetization-polarization coupling in Y-type hexaferrite crystals

V. Kocsis,<sup>1</sup> T. Nakajima,<sup>1</sup> M. Matsuda,<sup>2</sup> A. Kikkawa,<sup>1</sup> Y. Kaneko,<sup>1</sup> J. Takashima,<sup>1,3</sup>  
K. Kakurai,<sup>1,4</sup> T. Arima,<sup>1,5</sup> Y. Tokunaga,<sup>1,5</sup> Y. Tokura,<sup>1,6</sup> and Y. Taguchi<sup>1</sup>

<sup>1</sup>*RIKEN Center for Emergent Matter Science (CEMS), Wako, Saitama 351-0198, Japan*

<sup>2</sup>*Neutron Scattering Division, Oak Ridge National Laboratory, Oak Ridge, Tennessee 37831, USA*

<sup>3</sup>*Venture Lab TOKYO, NGK SPARK PLUG CO., LTD. Minato-ku, Tokyo 108-8243, Japan*

<sup>4</sup>*Neutron Science and Technology Center, Comprehensive Research*

*Organization for Science and Society (CROSS), Tokai, Ibaraki 319-1106, Japan*

<sup>5</sup>*Department of Advanced Materials Science, University of Tokyo, Kashiwa 277-8561, Japan*

<sup>6</sup>*Tokyo College and Department of Applied Physics,  
University of Tokyo, Hongo, Tokyo 113-8656, Japan*

Most of the Y-type hexaferrite materials family host a variety of magnetic structures as a ground state, and a multiferroic phase, termed FE3 phase, can be stabilized by applying magnetic ( $H$ ) field. This phase has recently been found to persist even after removing the  $H$  field. The magnetoelectric properties of Y-type hexaferrites are dominated mainly by the FE3 phase via the spin-driven electric polarization ( $P$ ). In the present study, the stability of the competing magnetic phases was investigated in Y-type hexaferrite compounds  $\text{Ba}_{2-y}\text{Sr}_y\text{Co}_2\text{Fe}_{12-x}\text{Al}_x\text{O}_{22}$  ( $x=0.9$ ) with Sr-doping levels of  $y=0.8, 1.0,$  and  $1.2$ . Combining the measurements of magnetization ( $M$ ),  $P$ , and neutron diffraction, we revealed the  $H$ - $T$  magnetic phase diagrams. It was found that the stability of the multiferroic FE3 phase is greatly improved in the Sr-rich compound. At room temperature, the FE3 phase in the Ba-rich compound is fragile against the removal of the  $H$  field, while it is robust in the Sr-rich compound, even for zero-field cooling. We also investigated the interplay between the  $P$  and  $M$  in the FE3 phase in the presence of both the high electric ( $E$ ) and  $H$  fields, and found that the coupling between  $P$  and  $M$  depends on the energy barrier separating the two magnetoelectric states. The energy barrier gradually decreases as the temperature is increased leading to the **reduction** of the  $P$ - $M$  coupling.

## I. INTRODUCTION

13

Recent advances in the research for novel multiferroics, which have (anti)ferroic order of both the electric polarization ( $P$ ) and magnetization ( $M$ ), have attracted great interest due to their potential for applications<sup>1-6</sup>. When the coupling between the  $P$  and  $M$  is strong, they can be manipulated by the application of magnetic ( $H$ ) and electric ( $E$ ) fields, respectively. This cross-coupling effect gives additional functionality to materials and thus anticipated to be employed in spintronic devices. Magnetization control by  $E$  field is of particular interest, as it may combine the high reliability of magnetic devices and the capability of high-speed electric manipulation with ultra-low power-consumption.

Multiferroics are often classified<sup>7</sup> into two groups according to the relationship between  $P$  and  $M$ . In type-I multiferroics,  $P$  typically emerges at higher temperatures and independently of the magnetic order, while in type-II multiferroics,  $P$  is produced by the spin order<sup>8-10</sup>. Heterostructures based on the type-I multiferroic BiFeO<sub>3</sub> have been considered to be the most promising candidates for applications **for a long time**, as the manipulation of magnetic domains by  $E$  field was demonstrated at room temperature<sup>11,12</sup>. However, in these materials the relationship between the magnetic and electric degrees of freedoms is not mutual; **although** the  $M$  is reversed to  $-M$  by the  $E$  field, the spin-driven  $P$  is an even function of the  $H$  field<sup>13</sup>, that is, not switched by the reversal of  $H$ . Among the type-II multiferroics, where the  $P$ - $M$  coupling is considered to be stronger than in type-I materials, the vast family of hexaferrite materials with versatile structural types have gained considerable interest<sup>4,5,14-17</sup>. In Z-type hexaferrite materials, multiferroic phases were observed at high temperatures and in small  $H$  fields. However, despite the high stability of the multiferroic phases, the magnetoelectric response is dominated mainly by a contribution which shows symmetric  $H$ -field dependence<sup>18,19</sup> (although, existence of a minor component with anti-symmetric  $H$ -field dependence has recently been identified<sup>19</sup>). In materials with symmetric  $P$ - $H$  and  $M$ - $E$  field dependence<sup>17</sup>, the reversal of  $P$  and  $M$  upon the reversal of the  $H$  and  $E$  fields are not expected. In Y-type hexaferrites, magnetoelectric responses with anti-symmetric field dependence were observed at low temperatures<sup>20-22</sup>.

In the phase diagrams of the Y-type hexaferrites, a large variety of non-collinear magnetic phases, both incommensurate and commensurate, can be realized by chemical doping. Among them, Sr- and Al-doping in the Ba<sub>2-y</sub>Sr<sub>y</sub>M<sub>2</sub>Fe<sub>12-x</sub>Al<sub>x</sub>O<sub>22</sub> ( $M$ =Mg, Co, Zn) proved to be an effective way to stabilize the multiferroic phases<sup>23-28</sup>. This has led to the realization of  $M$  switching by  $E$  field at low temperatures<sup>20,21</sup>. Moreover, a stable multiferroic phase termed FE3 phase was reported at room temperature in the Ba<sub>1.0</sub>Sr<sub>1.0</sub>Co<sub>2</sub>Fe<sub>11</sub>AlO<sub>22</sub><sup>27,28</sup>. In a previous paper<sup>29</sup>, we reported successful control of  $M$  by  $E$  and visualization of  $M$ -domain switching by  $E$  using magnetic force microscopy in a related compound near room temperature. This motivated us to systematically study the effect of Sr-doping on the magnetoelectric phases and responses in the Ba<sub>2-y</sub>Sr<sub>y</sub>Co<sub>2</sub>Fe<sub>12-x</sub>Al<sub>x</sub>O<sub>22</sub>. In this paper, we report the stability of the multiferroic phases with the change in the Ba/Sr ratio and investigate the robustness of  $P$ - $M$  coupling of the multiferroic phase.

45

## II. EXPERIMENTAL METHODS

Single-crystalline Y-type hexaferrites Ba<sub>2-y</sub>Sr<sub>y</sub>Co<sub>2</sub>Fe<sub>12-x</sub>Al<sub>x</sub>O<sub>22</sub> with  $x=0.9$  and  $y=0.8, 1.0, \text{ and } 1.2$  were grown by the laser floating-zone method<sup>30</sup>. Poly-crystalline precursor was prepared by solid state reaction of stoichiometric amounts of SrCO<sub>3</sub>, BaCO<sub>3</sub>, Co<sub>3</sub>O<sub>4</sub>, Fe<sub>2</sub>O<sub>3</sub> and Al<sub>2</sub>O<sub>3</sub> in air at 1150 °C for 24 h. The resulting product was pressed into rods and sintered for 14 h. Single crystals with  $\sim 10$  cm in length were grown in the laser floating-zone furnace in 10 atm oxygen atmosphere. The ingots were oriented with a back-scattering Laue camera and cut into discs with  $ac$  surfaces.

Resistivity of the as-grown samples are too low for high temperature magnetoelectric measurements<sup>29</sup>. To increase the resistivity, we followed Ref. [31] and performed a high-pressure O<sub>2</sub> annealing. The cut pieces were sealed in quartz tubes and annealed in 10 atm O<sub>2</sub> at 1000 °C for 100 h using Ag<sub>2</sub>O as oxygen source.

Neutron diffraction measurements were carried out for the O<sub>2</sub>-annealed single crystals at the triple-axis neutron spectrometer (PTAX) in the High Flux Isotope Reactor of Oak Ridge National Laboratory. The ( $H, 0, L$ ) plane was selected as a scattering plane, while the  $H$  field was applied perpendicular to the  $c$  axis (see Fig. 1).

For  $P$ - $H$  and  $M$ - $E$  measurements, single crystals with  $ac$  faces were polished and coated with Au/Pt electrodes. The  $E$  and  $H$  fields were applied perpendicular to each other and to the  $c$  axis ( $\mathbf{E} \perp \mathbf{H}$ ;  $\mathbf{E}, \mathbf{H} \perp c$ ). The  $P$  was obtained by measuring and integrating the displacement current with an electrometer (Keithley 6517A) while the  $H$  field was swept in a Physical Property Measurement System (PPMS, Quantum Design). The  $M$ - $T$  and  $M$ - $H$  measurements without  $E$  field were carried out in a Magnetic Property Measurement System (MPMS-3, Quantum Design). The  $M$ - $E$  and  $M$ - $H$  measurements under  $E$  field were performed by using a magnetometer (MPMS-XL, Quantum Design), while an electrometer (6517A, Keithley) was used as a voltage source. Prior to the measurements, single-domain magnetoelectric-state was prepared by the application of  $E_0=+5$  MV/m and  $H_0=+50$  kOe fields in the  $\mathbf{E} \perp \mathbf{H}$ ;  $\mathbf{E}, \mathbf{H} \perp c$  arrangement at the same temperature as the respective measurement temperature.

phase	wavevector	reflections
FiM	$q = 0$	(0,0,9), (1,0,4)
PH	$q = q_{1C}$	(0,0,9 $\pm q_{1C}$ ), (1,0,4 $\pm q_{1C}$ )
ALC	$q = q_{1C}$ , $q = 3/2$	(0,0,9 $\pm q_{1C}$ ), (1,0,4 $\pm q_{1C}$ ), (1,0,4 $\pm 3/2$ )
FE2'	$q = 3/4$ , $q = 0$	(0,0,9), (1,0,4), (0,0,9 $\pm 3/4$ ), (1,0,4 $\pm 3/4$ )
FE3	$q = 3/2$ , $q = 0$	(0,0,9), (1,0,4), (0,0,9 $\pm 3/2$ ), (1,0,4 $\pm 3/2$ )

TABLE I. Magnetic phases and their corresponding modulation vectors as well as the magnetic reflections used to identify the phases.

### III. STRUCTURE AND COMPETING MAGNETIC PHASES

The Y-type hexaferrites  $\text{Ba}_{2-y}\text{Sr}_y\text{Co}_2\text{Fe}_{12-x}\text{Al}_x\text{O}_{22}$  have a large structural unit cell (space group  $R\bar{3}m$ ) with hexagonal lattice constants  $a = a' \approx 5.8 \text{ \AA}$  and  $c \approx 43.3 \text{ \AA}$ , as shown in Fig. 1(a).  $\text{Fe}^{3+}/\text{Co}^{2+}$  and  $\text{Fe}^{3+}/\text{Al}^{3+}$  ions are either tetrahedral or octahedral ligand coordination<sup>16,32</sup>. The magnetic structure is known to be greatly simplified by employing block-spin approximation<sup>5,33-36</sup>. The magnetic moments of the  $\text{Fe}^{3+}/\text{Co}^{2+}$  ions constitute spin-blocks with small ( $S^S$ ) and large ( $S^L$ ) net magnetizations. Although the precise order within the blocks is unknown, they probably have a nearly collinear ferrimagnetic order<sup>33-35</sup>. The complete magnetic structure is composed of the alternate stacks of these two spin-blocks along the  $c$  axis.

In the Y-type hexaferrites, the Al-doping selectively replaces the  $\text{Fe}^{3+}$  ions at the octahedral sites<sup>15,37</sup>. By weakening both the super-exchange interactions and the easy-plane anisotropy, the Al-doping was found to suppress the coplanar incommensurate phases<sup>26</sup>. By contrast, as the Ba and Sr ions are located in between the  $S^S$  and  $S^L$  spin blocks, substituting Sr for Ba alters the Fe-O-Fe bond angles connecting the two blocks<sup>33-35</sup>. This leads to a change in the rotation angle between  $S^S$  and  $S^L$  block-spins, as well as to the prevalence of non-collinear magnetic structures with helical modulation. By doping with Al and Sr, we have access to different microscopic interactions and it is possible to stabilize a variety of non-collinear magnetic phases.

Figure 1(b,d) illustrates the relevant magnetic structures to this study, namely collinear ferrimagnetic phase (FiM), proper screw (PS), alternating longitudinal conical (ALC), as well as multiferroic FE2' and FE3 phases. In this paper, we follow the nomenclature introduced in Ref. [23]. The magnetic phases were identified using the representative  $(0,0,q)$  magnetic modulation wave vectors in the neutron diffraction profiles measured along the  $(0,0,L)$  and  $(1,0,L)$  lines<sup>5,28,36</sup>. In the present study, we focused on the  $L$  ranges of  $6 \leq L \leq 9$  and  $1 \leq L \leq 4$ , in the former and latter line scans, respectively. The assignment of the magnetic phases to the  $q$  modulation wavenumbers is summarized in Table I, while the details are discussed in the Supplementary Material<sup>38</sup>. The FiM phase is a collinear phase with uniform magnetization ( $q=0$ ) where  $S^S$  and  $S^L$  point to opposite directions, which can be viewed as a parent structure of all other phases. The PS phase has an incommensurate spiral order ( $q = q_{1C}$ ), with the magnetic moments confined within the  $ab$  plane due to the easy-plane anisotropy. The ALC phase has an incommensurate  $ab$ -plane component ( $q = q_{1C}$ ) similar to the PS phase, but the  $c$ -axis component of the moments shows commensurate modulation with  $q = 3/2$  along the  $c$  axis. In the FE2' structure ( $q = 3/4$ ), the  $S^L$  block-spins have a four-fold modulation<sup>36</sup>, which hosts ferroelectric polarization.

Among these magnetically ordered phases, the multiferroic FE3 phase has prominent significance as it appears in many Y-type hexaferrites and dominates the magnetoelectric properties<sup>5,27,28,36</sup>. The FE3 can be viewed as a double-fan structure with  $S^L$  and  $S^S$  lying within the  $ab$  and  $ac$  planes, respectively, as shown in Fig. 1(b). The FE3 structure can be also considered<sup>28</sup> as being composed of a staggered collinear ferrimagnetic component and an elliptical cycloidal one, that are parallel and perpendicular to the net  $M$ , respectively. The ferroelectric polarization is associated with the cycloidal component and emerges due to the spin-current mechanism<sup>8,39,40</sup>, perpendicular to both the net magnetization and  $c$  axis ( $\mathbf{P}, \mathbf{M} \perp c$  and  $\mathbf{P} \perp \mathbf{M}$ ). In the presence of the  $P$ - $M$  coupling, the four independent  $\pm M$  and  $\pm P$  states are reduced to two magnetoelectric states, labeled as  $\tau=+1$  and  $\tau=-1$ , as depicted

103 in Fig. 1(b,c). The  $\tau=+1$  magnetoelectric state means that the  $+P$  and  $-P$  states are coupled to the  $+M$  and  $-M$   
 104 states, respectively. On the other hand, the  $\tau=-1$  magnetoelectric state indicates the coupling between the  $+P$  and  
 105  $-M$  states, or  $-P$  and  $+M$  states. Here we note that due to the weak anisotropy within the  $ab$  plane<sup>29</sup>, the  $M$  and  
 106  $P$  may rotate within the  $ab$  plane nearly freely, while keeping the relative configuration of  $P$  and  $M$ , and hence the  
 107 magnetoelectric state, unchanged. In fact, this is the key for the  $M$  switching in this materials family<sup>20,28</sup>.

108 The angles between the  $S^L$  and  $M$ , and  $S^S$  and  $-M$  are denoted as  $\varphi^L$  and  $\varphi^S$ , respectively, as shown in Fig. 1(b).  
 109 The two magnetoelectric states of the FE3 phase differ in the relative phase between the  $S^L$  and  $S^S$  spin-blocks. For a  
 110 fixed phase of the large spin-block ( $\varphi^L > 0$ ), the magnetoelectric state  $\tau=+1$  corresponds to  $\varphi^S > 0$ , while the  $\tau=-1$   
 111 state has an opposite sign  $\varphi^S < 0$ . The magnetoelectric states can be changed with each other by interchanging the  
 112 signs of either of the  $\varphi^L$  or  $\varphi^S$  angles. The  $\varphi^L$  and  $\varphi^S$  angles are governed by the interplay between the exchange  
 113 couplings and anisotropies, thus they depend on the chemical composition, temperature, and magnetic field. The FE3  
 114 phase can be deformed into the FiM phase by tuning the angles to zero ( $\varphi^L = 0$ ,  $\varphi^S = 0$ ).

### 115 A. Phase diagram in the zero-field-cooled state

116 In this Section, we first describe the magnetic phases of the compound with equal Ba/Sr ratio ( $y=1.0$ ) using the  
 117 magnetization data in the low-field-cooled state and the neutron diffraction data collected for a zero-field-cooled (ZFC)  
 118 state in Fig. 2. Then, we proceed to compare the ZFC phase diagrams of the other two compounds and discuss the  
 119 impact of Sr-doping.

120 The ZFC magnetic phase diagram of the  $y=1.0$  compound is presented in Fig. 2(b), which was deduced from  
 121 the magnetization and neutron diffraction data shown in Figs. 2(e,h,k). Corresponding neutron diffraction profiles  
 122 measured along the  $(0,0,L)$  line are shown in Fig. S1 at selected temperatures. The  $y=1.0$  compound develops a  
 123 long-range collinear FiM order below  $T_{C1}=470$  K, which is identified by the onset of  $M$  for  $H \perp c$  ( $M_{\perp c}$ ) in Fig. 2(e)  
 124 as well as the increase in the integrated intensities of the  $(0,0,9)$  and  $(1,0,4)$  peaks, which are denoted as  $q=0$  in  
 125 Figs. 2(h,k). At  $T_{C2}=420$  K, the FiM phase is turned into the co-planar PS phase, which is indicated by the rapid  
 126 decrease in  $M_{\perp c}$ , the emergence of magnetic satellite peaks with  $q = q_{IC}$ , and the decrease in the intensities of the  
 127  $(0,0,9)$  and  $(1,0,4)$  peaks. Besides the incommensurate magnetic satellite peak, a commensurate modulation vector  
 128  $q = 3/2$  with small intensity also appears. This suggests the emergence of the FE3 phase co-existing with the PS  
 129 order as a minority phase. Finally, around  $T_{C3}=280$  K,  $M_{\perp c}$  shows a gradual increase, while the  $M$  for  $H \parallel c$  ( $M_{\parallel c}$ )  
 130 exhibits a kink. The ALC phase below  $T_{C3}$  is identified by the  $q = q_{IC}$  magnetic peak as well as the emergence of the  
 131 magnetic  $q=3/2$  peak along the  $(1,0,L)$  line, as shown in Fig. 2(k) and Table I. Here we note that the intensity change  
 132 across the boundaries between the ALC, PS, and FiM phases is gradual and continuous, suggesting the second order  
 133 nature of the phase transitions.

134 The magnetic phase diagram of the Ba-rich compound ( $y=0.8$ ) is rather similar to that of the  $y=1.0$  compound,  
 135 as shown in Fig. 2(a), and there are only minor differences. The onset of the FiM order is shifted towards higher  
 136 temperature ( $T_{C1}=485$  K) accompanied by the enhancement of the  $M_{\perp c}$ , while  $M_{\parallel c}$  is almost unchanged. As compared  
 137 to the  $y=1.0$  compound, the intensity of the  $q=3/2$  magnetic peak along the  $(0,0,L)$  line is much reduced, except for a  
 138 narrow temperature region around  $T_{C2}$  [Fig. 2(g)]; the FE3 phase is almost completely destabilized in this compound.  
 139 The boundaries between the FiM, PS, and ALC phases ( $T_{C2}$  and  $T_{C3}$ ) are roughly the same as those in the  $y=1.0$   
 140 compound.

141 The Sr-rich compound ( $y=1.2$ ) has a substantially different ZFC phase diagram than the other two compounds, as  
 142 reproduced in Fig. 2(c) from Ref. [29]. The most important difference is the co-existence of multiple magnetic phases,  
 143 which was verified at  $T=295$  K by using magnetic force microscope in the earlier study<sup>29</sup>. Besides the FiM order, the  
 144 multiferroic FE3 phase with  $q=3/2$  appears at  $T_{C1}=450$  K, as shown in Fig. 2(i,l). While the FiM phase is replaced  
 145 by the PS and FE2' phases at  $T_{C2}=400$  K, the latter of which is identified with the  $q=3/4$  magnetic reflection, the  
 146 FE3 phase persists down to low temperatures. Notably,  $M_{\perp c}$  does not decrease substantially below  $T_{C2}$  as compared  
 147 with  $y=0.8$  and  $1.0$  compounds, which is an indication of the stable FE2' and FE3 phases. Finally, at  $T_{C3}=300$  K  
 148 the PS is replaced by the ALC phase. The increase in the  $M_{\perp c}$  below  $T_{C3}$  is probably related to the FE2' and FE3  
 149 phases rather than to the ALC phase.

150 The phase transition temperatures of all the three compounds are summarized in Table II, while the Ba/Sr-ratio  
 151 dependence of the  $q_{IC}$  in the incommensurate ALC and PS phases are shown in Fig. S2. The  $q_{IC}$  has non-monotonous  
 152 temperature dependence, and the periodicity of the modulation is increased as the Sr-doping level is increased. To  
 153 give a more intuitive picture for the effect of Sr-doping on  $q_{IC}$ , we note that the turn angle between two neighboring  
 154  $S^L$  block-spins along the  $c$  axis is increased from  $95^\circ$  for  $y=0.8$  to  $120^\circ$  for  $y=1.2$ , at  $T=300$  K.

$y$	$T_{C1}$ (K)	$T_{C2}$ (K)	$T_{C3}$ (K)	$T_1$ (K)	$T_2$ (K)
0.8	485	410	285	200	275
1.0	470	420	280	280	340
1.2	450	400	300	280	450

TABLE II.  $T_{C1}$ ,  $T_{C2}$ , and  $T_{C3}$  are the magnetic phase transition temperatures that separate the PM (paramagnetic), FiM (collinear ferrimagnetic), PS (proper-screw), and ALC (alternating longitudinal conical) phases, respectively. At low temperature the FE3 phase is stabilized in the presence of high  $H_{\perp c}$  field and preserved when the field is removed.  $T_1$  is the temperature above which the FE3 phase becomes only partially stable in the absence of  $H_{\perp c}$  field, *i.e.* the FE2' and ALC/PS phases reappear.  $T_2$  is the highest temperature where the FE3 phase can be observed after removing the  $H_{\perp c}$  field.

## B. Magnetic phases in $H \perp c$ field

In the previous Section, we have discussed the ZFC magnetic phase diagram of Sr-doped Y-type hexaferrites. In this Section we proceed to discuss the phase diagram as a function of applied field ( $\mathbf{H} \perp c$ ) at room temperature. Following the temperature-dependent phase diagrams, we start with the description for the  $y=1.0$ , then we compare the other two compounds with lower and higher Sr-doping levels.

The  $H_{\perp c}$  field-dependent neutron scattering measurement for the  $y=1.0$  compound was started from the ZFC state at  $T=295$  K. In agreement with the earlier reports on similar compounds<sup>27,28,37</sup>, the PS phase with  $q_{IC}=0.89$  modulation is stabilized in the initial ZFC state, as shown in Fig. 3. A small peak is observed at  $L=7.5$  ( $q=3/2$ ) in Fig. 3, which indicates the presence of FE3 phase as a minority phase. Upon the application of  $H$  field perpendicular to the  $c$  axis, the magnetic reflections with  $q_{IC}$  disappear and the intensity at  $L=7.5$  ( $q=3/2$ ) significantly increases for  $H=3$  kOe. According to more detailed field-dependence [see Fig. 4(h,k,n)], the PS phase is completely replaced by the FE3 phase at around  $H=0.9$  kOe. When the  $H_{\perp c}$  field is removed, the intensity of the  $q=3/2$  reflection decreases to almost half, compared to that at 3 kOe, that is, the FE3 phase is only partially preserved. Besides the change in the  $q=3/2$  reflection, a new, asymmetric magnetic peak emerges around  $q=0.77$ , which is close to the  $q=3/4$  of the FE2' phase. The change in the shape and position of the magnetic peak suggests the mixture of the coexistent PS and FE2' phases, rather than the restoration of the PS phase with a field-history-dependent, slightly different  $q_{IC}$  modulation vector. The analysis of the scattering intensity in terms of the PS and FE2' phases is detailed in Fig. S3<sup>38</sup>.

The integrated intensity of representative peaks is plotted as a function of applied field in Figs. 4(h,k,n). In the low-field region ( $H < 1$  kOe), the field variation of the integrated intensities can be attributed to the change in volume fraction of the magnetic phases, rather than deformation of the magnetic structures. The FE3, FE2', and PS phases are therefore represented by the integrated intensities of the  $q=3/2$ ,  $q=3/4$ , and  $q_{IC}$  magnetic reflections on the  $(0,0,L)$  line shown in Figs. 4(h), 4(k), and 4(n), respectively. When the  $H_{\perp c}$  field is reversed to negative, the intensity of the  $q=3/2$  peak has its minimum exactly where the PS and FE2' phases have their maximum intensities. Towards even higher negative  $H$  fields, the PS phase first disappears at around  $H=-0.9$  kOe, then FE2' phase does at  $H=-1.0$  kOe, and the FE3 phase is again fully stabilized. Here the FE2' phase is stable up to higher  $H_{\perp c}$  fields and occupies larger region in the phase diagram than the PS phase. In Fig. 4(e), field dependence of magnetization ( $M_{\perp c}$ ) is presented. The PS phase shows a small magnetization for  $H_{\perp c}$  while the FE3 phase has a large ferrimagnetic moment. The field dependence of  $M$  is understood in accord with the neutron intensity change.

Figure 4(b) shows the magnetic phase diagram of  $y=1.0$  based on the neutron and magnetization measurements in the field-increasing run after ZFC (first line) and in the subsequent field-decreasing run (second line). The boundaries in the phase diagram were determined on the basis of the anomalies in the  $M-H_{\perp c}$  measurement displayed in Fig. 4(e), while the phases were identified using the results of neutron diffraction that are shown in Fig. 4(h,k,n).

As shown in Fig. 4(a), the room-temperature ZFC state of the Ba-rich compound ( $y=0.8$ ) is the PS phase, similarly to the  $y=1.0$  compound. Details of the refinement of the neutron diffraction data are discussed in the Supplementary Material. Compared to the  $y=1.0$  compound, the PS phase is replaced by the FE3 phase more gradually between  $H=0.5$  kOe and 1.2 kOe for the first application of magnetic field, as shown in Fig. 4(g,j,m), which is accompanied by a step in the  $M-H$  curve in Fig. 4(d). Moreover, within the same magnetic field region, the intensity for the FE2' phase also increases, showing a peak at  $H=1.0$  kOe. The disappearance of the FE2' phase coincides with a secondary step-like feature in the  $M-H$  curve in Fig. 4(d). In the field-decreasing run, the FE3 phase is again gradually replaced by the FE2' and PS phases. First the FE2' phase emerges at  $H=0.7$  kOe, then the FE2' phase partially turns into the PS phase below  $H=0.3$  kOe. In the absence of magnetic field the FE3 phase is not stable and it re-appears only below  $H=-0.5$  kOe. Upon further decreasing the  $H$  field, the FE3 phase is restored from the PS and FE2' phases at  $H=-1.0$  kOe and  $H=-1.2$  kOe, respectively.

The Sr-rich compound ( $y=1.2$ ) hosts all the three phases in its ZFC state at room temperature, as shown in Fig. 4(c). The FE3 phase is stable and the application of the  $H=0.7$  kOe field doubles the integrated intensity of

the corresponding  $q=3/2$  peak, as shown in Fig 4(i). The FE2' and PS/ALC phases are replaced by the FE3 phase at  $H=0.7$  kOe and  $H=1.0$  kOe fields, respectively [Figs. 4(l) and 4(o)]. The phase transition is accompanied by a step in the  $M$  [Fig. 4(f)]. In the field-decreasing run, the FE3 phase is only partially replaced by the FE2' and PS phases, similarly to the  $y=1.0$  compound. The FE2' phase reappears between  $H=0.4$  kOe and  $H=-0.9$  kOe, while the PS/ALC phase does between  $H=0.1$  kOe and  $H=-0.8$  kOe field range.

### C. The $H_{\perp c}$ - $T$ magnetic phase diagram

Figures 5(a-c) compare the  $H_{\perp c}$ - $T$  magnetic phase diagrams of all the three compounds in the field-increasing runs after ZFC, while Figs. 5(d-f) show those obtained in the field-decreasing experiments. The phase boundaries were determined by using the anomalies in the low-field  $M$ - $T$  data and in the field derivatives of the isothermal  $M$ - $H$  curves. The magnetic phases were assigned according to their magnetic peaks (see Table I) observed in the neutron diffraction measurements. Isothermal  $M$ - $H_{\perp c}$  curves at selected temperatures are shown in Fig. S4.

In the compounds with  $y=0.8$  and  $y=1.0$ , the FiM, PS, and ALC phases are stabilized for the ZFC below  $T_{C1}$ ,  $T_{C2}$ , and  $T_{C3}$ , respectively, as shown in Fig. 5(a,b). By contrast, in the  $y=1.2$  compound the coexisting states of FiM/FE3, PS/FE2'/FE3, and ALC/FE2'/FE3 are found below the corresponding temperatures in Fig. 5(c). In each compound, the application of  $H_{\perp c}$  field favors the FE3 phase exclusively. The magnitude of the  $H_{\perp c}$  field to stabilize the FE3 phase decreases towards higher temperatures. For even higher  $H_{\perp c}$  field in the FE3 phase, the angles between the  $S^S$ - $S^S$  and  $S^L$ - $S^L$  block-spin pairs gradually decrease, and the double-fan structure is finally turned into the collinear FiM structure.

In the  $H_{\perp c}$ -decreasing processes shown in Fig. 5(d-f), the FE3 phase is restored from the high-field FiM phase. When the  $H_{\perp c}$  field is removed at low temperature, the FE3 phase is fully preserved in each compound. However, in an intermediate temperature region that depends on the Sr concentration, the FE3 phase is only partially preserved, and above this temperature region, the FE3 phase is unstable. In the absence of  $H_{\perp c}$  field, the FE3 phase in the  $y=0.8$  compound is partially stable above  $T_1=200$  K and unstable above  $T_2=275$  K as shown in Fig. 5(d). In case of the  $y=1.2$  compound [Fig. 5(f)], the FE2' and ALC phases reappear only around  $T_1=280$  K while the FE3 phase is partially preserved up to  $T_2=450$  K. These temperatures representing the stability of the FE3 phase are summarized in Table II. Here we note that upon the reversal of the  $H_{\perp c}$  field, the FE3 phase is turned into the FE2' or ALC phases at even lower temperatures than  $T_1$  as discussed in Ref. [29]. This suggests that the transition between the FE3 and ALC/PS phases might be related to magnetic domain walls that appear in the course of magnetization reversal; namely the ALC/PS phase can nucleate at magnetic domain walls of the FE3 phase.

### D. Summary of the magnetic phase diagram

In the Y-type hexaferrites  $\text{Ba}_{2-y}\text{Sr}_y\text{Co}_2\text{Fe}_{12-x}\text{Al}_x\text{O}_{22}$  ( $y=0.8, 1.0, \text{ and } 1.2$ ), Sr-doping stabilizes the multiferroic FE3 phase. As discussed in relation with Fig. 4, the FE3 phase is unstable, meta-stable, and partially stable at room temperature in the  $y=0.8, 1.0, \text{ and } 1.2$  compounds, respectively. Apart from the effect on the FE3 phase, Sr-doping destabilizes the ferrimagnetic (FiM) and proper-screw (PS) phases, as their temperature regions in the phase diagram are reduced (Fig. 5). Sr-doping favors the magnetic phases with non-coplanar structure, such as the alternating longitudinal conical (ALC), FE2', and FE3 phases. Increasing the Sr-doping gradually decreases the  $T_{C1}$ , suggesting the reduction of the strong antiferromagnetic coupling between the  $S^S$  and  $S^L$  block-spins.

The realization and stability of the FE3 phase at low temperature are discussed by using a schematic illustration of a possible free energy diagram in Fig. 6(a) for the  $y=0.8$  compound as an example. Here we note that these free energy diagrams are phenomenologically introduced to interpret the observed first order transitions, based on the magnetization and neutron diffraction data, and not on a model calculation, which appears to be difficult in view of the complicated magnetic structures. The zero-field-cooling (ZFC) stabilizes the incommensurate ALC phase, therefore this state has the lowest free energy in the phase space of the order parameters (represented by a horizontal axis for the purpose of simplicity). In the presence of  $H_{\perp c}$  field, the free energy of the FE3 phase with a large magnetization is lowered, while the free energy of the ALC phase with a small magnetization is almost unchanged. In sufficiently large  $H_{\perp c}$  field, the energy barrier separating the FE3 and ALC phases diminishes, and the incommensurate ALC phase is completely turned into the multiferroic FE3 phase. When the  $H_{\perp c}$  field is removed, the energy barrier is restored, and the FE3 phase is stabilized as a meta-stable state<sup>28</sup>. At sufficiently low temperature, the energy barrier is large enough to protect the meta-stable FE3 phase against the thermal agitation. Increase in temperature reduces the energy barrier, making the FE3 phase less stable, and the incommensurate ALC or PS phases more stable. This well accounts for the experimental observations shown in Fig. 5. As the temperature is increased, smaller  $H_{\perp c}$  field

is needed to drive the ALC/PS phases into the FE3 phase, and in turn the FE3 phase more easily returns back into the ALC/PS phases in the field-decreasing runs.

Due to the several competing energies, co-existing multiferroic phases, such as the FE1, FE2, FE2', and FE3, are commonly observed in Y-type hexaferrites<sup>5,15,23,26,36</sup>. In this respect, Fig. 6(b) illustrate a possible interpretation for the role of the FE2' phase, taking an example of the  $y=0.8$  compound. Moderate field of  $H_{\perp c}=1.5$  kOe stabilizes the FE3 phase at  $T=300$  K, while the FE2' and PS phases are unstable. As the  $H_{\perp c}$  field is decreased to 400 Oe, both the PS and FE2' phases are regarded as meta-stable states with higher free energy than the FE3 phase. While the energy barrier between the PS and FE3 phases is still sufficiently large, the barrier between the FE2' and FE3 phases becomes small and the FE2' phase appears. When the  $H_{\perp c}$  field is removed, the FE3 phase is destabilized, and the energy barrier between the PS and the FE2'/FE3 phases vanishes, stabilizing the PS phase. In this scenario, the FE2' phase takes the role of an intermediate state, which bridges the FE3 and PS/ALC phases.

In the  $y=0.8$  compound, the FE2' phase may greatly reduce the energy barrier between the FE3 and ALC phases, thereby destabilizing the FE3 phase. In the  $y=1.2$  compound, on the contrary, the energy landscape changes and the meta-stability of the FE3 phase is preserved, as schematically shown in Fig. 6(c).

#### IV. MAGNETIZATION-POLARIZATION COUPLING IN EXTERNAL FIELDS

The existence of a stable multiferroic phase is a necessary condition for the  $E$ -field control of the ferromagnetic moment, however not yet a sufficient one, as discussed for Z-type hexaferrites as an example in the Introduction. In multiferroic compounds, magnetoelectric domains can form where the  $M$  and  $P$  have different coupling, say  $\tau=+1$  or  $\tau=-1$  coupling as exemplified for Y-type hexaferrites in Figs. 1(b,c). These states have the same energy in the absence of external fields, and show responses with opposite sign to the external field. Therefore, in a multi-domain sample, the overall magnetoelectric response is compensated. Application of external  $E$  and  $H$  fields (magnetoelectric poling) can stabilize one of these states and then finite magnetoelectric response can emerge. In addition, the magnetoelectric state has to be robust against external stimuli; namely, once an magnetoelectric state is selected, it should be hardly changed into the other state. This suggests that these states have to be well separated from each other by a large energy barrier. To understand the coupling in detail, we selectively alter the electric or magnetic energy by applying external fields, and investigate the magnetic as well as the magnetoelectric properties.

##### A. Direct and converse magnetoelectric responses

First, the direct and the converse magnetoelectric responses were studied using the isothermal  $P$ - $H$  and  $M$ - $H$  measurements, shown in Figs. 7 and S5<sup>38</sup>. Both types of measurements were conducted for a single-domain magnetoelectric state, prepared by the application of large  $E$  and  $H$  fields in the  $\mathbf{E} \perp \mathbf{H}$ ;  $\mathbf{E}, \mathbf{H} \perp c$  geometry. To obtain the  $P$ - $H$  loops, pyrocurrent was measured in the absence of  $E$  field while the  $H$  field was cyclically swept between  $\pm 5$  kOe for 17-50 times. The  $M$ - $E$  measurements were performed after carefully removing the  $H$  field, while the  $E$  field was swept between  $\pm 5$  MV/m. As shown in Figs. 7(a)-7(f), the FE3 phase is stable at  $T=250$  K and the  $P$ - $H$  as well as the  $M$ - $E$  loops exhibit anti-symmetric field dependence. This demonstrates that the prepared magnetoelectric state is stable, that is,  $P$  and  $M$  are strongly coupled, and the  $H(E)$  field cannot change the  $M(P)$  state without switching the  $P(M)$  state. The saturation value of the  $P$  depends on the Ba/Sr ratio, and it increases from  $P_{\text{H}}^{\text{sat}}=150 \mu\text{C}/\text{m}^2$  for  $y=0.8$  to  $P_{\text{H}}^{\text{sat}}=250 \mu\text{C}/\text{m}^2$  for  $y=1.2$ . Accordingly, the  $H$  field needed to saturate the  $P$ , increases from  $H^{\text{sat}}=250$  Oe for the Ba-rich compound ( $y=0.8$ ) to  $H^{\text{sat}}=600$  Oe in the Sr-rich compound ( $y=1.2$ ).

In contrast to the  $P$ - $H$  experiments, the  $M$ - $E$  loops are incomplete and the magnitudes of  $M$  decrease for every cycle of the  $E$  field application at 250 K. Despite the large  $E$  field, saturation of  $M$  is clearly not reached, and the samples show characteristic feature of fatigue. Nevertheless, the largest changes in the  $M$  are achieved in the  $y=0.8$  and 1.2 compounds. The coercive  $E_{\text{C}}$  field is the smallest in the Ba-rich compound, which explains the large magnitude of the magnetization change  $\Delta M_{\text{E}}^{\text{s}}=5.5 \mu_{\text{B}}/\text{f.u.}$  for the application of  $\pm 5$  MV/m fields [for the definition of  $\Delta M_{\text{E}}^{\text{s}}$ , see Fig. 8(e)]. By contrast, although the  $E_{\text{C}}$  is the largest in the Sr-rich compound, the large magnitude of  $\Delta M_{\text{E}}^{\text{s}}=4.5 \mu_{\text{B}}/\text{f.u.}$  is achieved, which is rather ascribed to the stronger  $P$ - $M$  coupling. In each compound, the remanent values of the  $P$  and  $M$  are the fraction of their respective saturation values, suggesting the formation of  $P$ - and  $M$ -domains. However, within a domain, the  $P$  and  $M$  are strongly coupled together, namely, the  $P$  and  $M$  domain walls are confined and the magnetoelectric state is preserved, probably even within the domain walls.

Figure 8 compares the temperature dependence of representative quantities related to the magnetoelectric responses ( $P_{\text{H}}^{\text{rem}}$ ,  $P_{\text{H}}^{\text{sat}}$ ,  $\Delta M_{\text{E}}^{\text{r}}$ , and  $\Delta M_{\text{E}}^{\text{s}}$ ) for all the three compounds. Figure 8(a) shows the definition for the remanent value of the polarization,  $P_{\text{H}}^{\text{rem}}$ , while the  $P_{\text{H}}^{\text{sat}}$  is defined as the maximum of the  $P$ - $H$  loops, which is different from the high-field limit. The quantity  $\Delta M_{\text{E}}^{\text{r}}$  has prominent technological significance, as it measures the change in the non-volatile



303  $M$  for the first cycle of the  $E$  field, as defined in Fig. 8(e). As the saturation is not reached in the  $M$ - $E$  experiments,  
 304 we can only define the change in the  $M$  for the application of  $\pm 5$  MV/m fields,  $\Delta M_E^s$ , as illustrated in Fig. 8(e).  
 305 For all the three compounds,  $P_H^{\text{sat}}$  as well as  $P_H^{\text{rem}}$  decreases towards higher temperatures, in contrast to  $\Delta M_E^s$  and  
 306  $\Delta M_E^r$  which exhibit non-monotonous temperature dependence. At 300 K, the  $P$ - $H$  and  $M$ - $E$  loops become small  
 307 with saturation values of  $P_H^{\text{sat}}=10\text{-}50 \mu\text{C}/\text{m}^2$  and  $\Delta M_E^s=0.25 \mu_B/\text{f.u.}$ , respectively. The non-monotonous behavior of  
 308  $\Delta M_E^s$  and  $\Delta M_E^r$  is most prominent in case of the  $y=0.8$  compound, where these changes increase up to a maximum  
 309 value of  $\Delta M_E^s=6.0 \mu_B/\text{f.u.}$  at  $T=240$  K, then drops to zero before reaching  $T=300$  K. The temperature dependence  
 310 of  $\Delta M_E^s$  and  $\Delta M_E^r$  is partly ascribed to that of the coercive  $E_C$  field, shown in Fig. S7(a-c). Between  $T=200$  K and  
 311 240 K,  $E_C$  decreases as  $T$  is increased and therefore it is easier to switch the  $M$  domains using  $E$  field. However, as  
 312 the temperature is further increased, the  $P$ - $M$  coupling is lost and the  $\Delta M_E^s$  and  $\Delta M_E^r$  approach to zero. In addition  
 313 to the reduced magnitudes, the  $P$ - $H$  and  $M$ - $E$  loops at room temperature indicate the emergence of substantial  
 314 contributions with symmetric field dependence, *i.e.* the appearance of butterfly shaped  $P$ - $H$  and  $M$ - $E$  curves, shown  
 315 in Fig. S5. The symmetric  $P$ - $H$  loop implies that the reversal of  $H$  field switches the magnetoelectric state, instead  
 316 of the  $P$  state, hence that the magnetoelectric state is not robust against external field.

### 317 B. Magnetic phases in the presence of $E$ and $H$ fields

318 The re-appearance of the incommensurate phases (**proper-screw (PS)** or **alternating longitudinal conical (ALC)**)  
 319 close to room temperature is a serious issue which hinders the  $E$ -field control of the magnetization in the Y-type  
 320 hexaferrite compounds. It is important to investigate the conditions with which the ALC or PS phases can be  
 321 suppressed. Figure 9(a) compares the  $M$ - $H$  loops for the  $y=1.0$  sample in multi- and single-domain magnetoelectric-  
 322 states at  $T=275$  K. The multi-domain state (orange curve) is obtained by heating the sample up to  $T=380$  K and  
 323 then cooling in zero field. The  $M$ - $H$  curve starts from the ALC phase at 0 kOe (1) with a low initial slope of  $M$ .  
 324 In agreement with the former measurements shown in Fig. 5, the ALC phase is replaced by the FE3 phase around  
 325 0.9 kOe, which is signaled by a jump in the  $M$ . When the  $H$  field is swept back and reversed (2), the ALC phase  
 326 partially re-emerges around  $-0.15$  kOe and again vanishes around  $-0.9$  kOe. In the second field-increasing run (3),  
 327 the re-emergence of the ALC phase in the positive low- $H$  region is observed. Next, the single-domain magnetoelectric-  
 328 state is prepared by the application of large poling  $E$  and  $H$  fields ( $E_0=+5$  MV/m,  $H_0=+50$  kOe) in the  $\mathbf{E} \perp \mathbf{H}$ ;  
 329  $\mathbf{E}, \mathbf{H} \perp c$  geometry at 275 K, and the  $M$ - $H$  measurement is started from high  $H$  field in the absence of  $E$  field  
 330 (black dashed curve). In this case the ALC phase with small magnetization is not observed, while the FE3 phase  
 331 is preserved throughout the  $M$  switching process. Thus, in the single-domain magnetoelectric-state, formation of  
 332 non-magnetoelectric phases is greatly suppressed.

333 A possible explanation for these features is schematically illustrated in Fig. 9(b). In the sample without  
 334 magnetoelectric poling, there are many domain boundaries in contrast to the poled case. At the magnetoelectric  
 335 domain walls, the  $P$  forms a head-to-head or tail-to-tail configuration with increased electro-static energy, which may  
 336 serve as a seed for the formation of the non-polar ALC phase, in accord with the observation by recent studies<sup>29,41</sup>.  
 337 In the multi-domain magnetoelectric-state, the ALC domains can expand into a macroscopic phase, while in the  
 338 single-domain case, there is no such domain wall to be a seed for the ALC phase. Further differences of magnetic  
 339 properties between the multi- and single-domain magnetoelectric-states are illustrated in Fig. S7(d-i) for all the three  
 340 materials.

341 When the  $E$  and  $H$  fields are simultaneously applied for coupled  $P$ - $M$  domains of a multiferroic material,  $E$ -field  
 342 biasing for the  $M$ - $H$  hysteresis loop can be observed<sup>22,42,43</sup>. In Fig. 10, we demonstrate this effect for the  $y=1.0$  sample  
 343 at  $T=200$  K. The fields were applied in the  $\mathbf{E} \perp \mathbf{H}$  and  $\mathbf{E}, \mathbf{H} \perp c$  geometry. Prior to the  $M$ - $H$  measurements, the sample  
 344 was poled into a single-domain  $\tau=+1$  magnetoelectric state using  $(+E_0, +H_0)$  fields ( $E_0=5$  MV/m,  $H_0=50$  kOe). When  
 345 no  $E$  field is applied, the  $M$ - $H$  loop of the single-domain sample is centered at  $H=0$  (dashed black curve) as shown  
 346 in Fig. 10(a). Upon applying  $E > 0$  (red curve) or  $E < 0$  (blue curve) fields, the  $M$ - $H$  loop shifts towards the  
 347  $-$  or  $+$  direction of the  $H$ -field axis, respectively. Schematic explanation for the  $E$ -biased  $M$ - $H$  loop is provided  
 348 in Figs. 10(b-e). In the  $\tau=+1$  state, the  $+P$  and  $-P$  states are clamped with the  $+M$  and  $-M$  magnetic states,  
 349 respectively. In the presence of  $E > 0$  field, the  $(+P, +M)$  state has a lower free energy by  $2 P \cdot E$  in the absence of  
 350  $H$  field, as shown in Fig. 10(b). When the coupling is strong,  $P$  and  $M$  cannot be switched independently. To switch  
 351 the magnetic state, the dielectric part of the free energy  $2 P \cdot E$  has to be compensated by the application of a larger  
 352 coercive field  $H_C(E)$ . Therefore, the  $M$ - $H$  loop is shifted to the  $-H$  direction [Fig. 10(c)]. On the contrary, when  
 353  $E < 0$  field is applied, the free energy of the  $(+P, +M)$  state is higher by  $2 |P \cdot E|$ , and the  $M$ - $H$  loop is shifted to  
 354 the  $+H$  direction, as shown in Fig. 10(d,e).

355 At low temperatures, the magnetic coercive fields  $H_{C+}$  and  $H_{C-}$  for the  $H$ -increasing and decreasing runs,  
 356 respectively, exhibit linear  $E$ -field dependence, as shown in Fig. S8. At high temperatures, however, the  $H_{C\pm}(E)$   
 357 coercive fields show more complex  $E$ -field dependence. Figures 11(a,b) display  $E$ -field biased  $M$ - $H$  loops measured

358 at  $T=275$  K, while the  $E$ -field dependence of the  $H_{C\pm}$  is presented in Fig. 11(c). The measurements were started  
 359 from the single-domain  $\tau=+1$  magnetoelectric state, similarly to the earlier cases. As shown in Fig. 11(c), when  
 360 the magnitude of the  $E$  field is small, the  $M$ - $H$  hysteresis loops are shifted in proportion to the applied  $E$  field,  
 361 in the same way as the low-temperature measurements presented in Figs. 10 and S8. However, when large  $E$  fields  
 362 are applied, the linear dependence of  $H_{C\pm}$  on  $E$ -field does not hold any more, and the hysteresis loop is widened  
 363 instead of shifted. Besides, as indicated by shoulder-like structures at  $0.2\text{kOe} \leq |H| \leq 0.8\text{kOe}$ , the ALC phase  
 364 reappears even when the sample was initially poled to a single-domain magnetoelectric state, in contrast to the case  
 365 shown with a dashed-line in Fig. 9(a). The widening of the hysteresis loop, and hence the deviation of  $H_{C\pm}(E)$  from  
 366 linear-dependence, suggests the switching between the  $\tau=+1$  and  $\tau=-1$  states. In the presence of  $E > 0$  and  $H < 0$   
 367 fields with high absolute values, the original  $\tau=+1$  state is turned into the  $\tau=-1$  state to gain both the electrostatic  
 368 energy and the Zeeman energy. Therefore, in the subsequent  $H$ -increasing run from negative to positive field, the  
 369  $H_{C+}$  is shifted to larger positive fields due to the reversed  $P$ - $M$  coupling. The re-emergence of the non-polar ALC/PS  
 370 phases in the presence of  $E$  and  $H$  fields is more clearly demonstrated in Fig. S9.

### 371 C. Investigation of the $P$ - $M$ coupling

372 The switching between the  $\tau=+1$  and  $\tau=-1$  magnetoelectric states in the  $E$ -field biased  $M$ - $H$  measurements at  
 373 high temperatures (Fig. 11) motivated us for further experiments, namely  $E$ -field biased  $P$ - $H$  measurements. This  
 374 experiment may provide a more reliable information on the  $P$ - $M$  coupling than the differential magnetoelectric  
 375 susceptibilities, often used in literature<sup>11,12,15,20,21</sup>. In multiferroic materials, the differential magnetoelectric  
 376 susceptibilities, defined as  $\partial P/\partial H$  and  $\partial M/\partial E$ , are dominated by domain switching effects at low fields, similarly to  
 377 the  $\partial M/\partial H$  susceptibility in ferromagnets.

378 Figures 12(a,b) show  $P$ - $H$  loops for  $y=1.2$  at  $T=200$  K with a complete cycle of the  $H$ -field for two different values of  
 379 the applied  $E$  field. The  $E$  and  $H$  fields are in the  $\mathbf{E} \perp \mathbf{H}$  and  $\mathbf{E}, \mathbf{H} \perp c$  configuration. In Fig. 12(a), the measurement  
 380 is started from  $H=+60$  kOe in the collinear FiM phase (where  $P$  is zero), in the presence of small  $E=+0.5$  MV/m field.  
 381 As the  $H$  field is decreased below  $H=+42$  kOe to enter into the FE3 phase, the sample is poled to a single-domain  
 382 magnetoelectric-state with  $\tau=+1$ , and  $P > 0$  emerges. When the  $H$  field is reversed to negative, the  $M$  as well as the  
 383 coupled  $P$  is reversed to negative, while keeping the  $\tau=+1$  state. As the field approaches  $H=-42$  kOe, the FE3 phase  
 384 is turned again into the FiM phase and the field-induced  $P$  vanishes. When the  $H$  field is increased from negative  
 385 to positive, a similar  $P$ - $H$  curve is observed with the opposite sign of  $P$ , as in this case the combination of  $E > 0$   
 386 and  $H < 0$  fields selects the  $\tau=-1$  magnetoelectric state; The FE3 phase re-appears at  $H=-42$  kOe with positive  
 387  $P$ , which is reversed to negative at  $H=0$  kOe and disappears again at  $H=42$  kOe field.

388 However, in the presence of high  $E=+4.5$  MV/m field, the  $P$ - $H$  loop exhibits different behavior, as shown in  
 389 Fig. 12(b). In the field-decreasing run, after the  $P$  is once switched to negative around  $H=0$ , the  $P$  is switched back to  
 390 positive within the FE3 phase before reaching the FE3-FiM phase boundary. This corresponds to the magnetoelectric  
 391 state switching from  $\tau=+1$  to  $\tau=-1$ . The isothermal switching between the  $\tau=+1$  and  $\tau=-1$  states is more clearly  
 392 demonstrated in Fig. 12(c) at a lower temperature,  $T=100$  K; a schematic illustration for the switching process is  
 393 provided in Fig. 12(d).

394 Similar measurements at 200 K with changing the  $E$  field reveal a first-order boundary between the two  
 395 magnetoelectric states of the FE3 phase, as shown in Fig. 13(a). The coercive field  $H_C^{\text{ME}}$  corresponds to the switching  
 396 from the  $\tau=-1$  to  $\tau=+1$  state for a given value of the  $E$  field [for definition, see the caption of Fig. 12(d)]. At  
 397  $T=200$  K,  $E < 3$  MV/m field is insufficient and results in partial switching, *i.e.* only a tiny portion is reversed in terms  
 398 of the magnetoelectric state. For higher  $E$  fields, the  $H_C^{\text{ME}}$  decreases.

399 Figure 13(b) shows the temperature dependence of the coercive field  $H_C^{\text{ME}}$  in the  $H$ -increasing run for an applied  $E$ -  
 400 field of  $+4.5$  MV/m. The displacement current measurement under such high  $E$ -field is possible only up to  $T=220$  K,  
 401 above which the current peaks of magnetic origin are masked out by large background noise. For comparison, the  
 402 FE3-FiM phase boundary is also shown in the  $H$ -increasing runs. It is noted that the  $H_C^{\text{ME}}$  may be affected by domain-  
 403 pinning effects, as well as by the proximity to the FiM phase. The  $H_C^{\text{ME}}$  field monotonously decreases towards higher  
 404 temperatures. This means that as the temperature is elevated, the  $\tau=+1$  magnetoelectric states can be switched  
 405 by the application of both smaller  $E$  and  $H$  field, and that they are fragile against external stimuli and thermal  
 406 agitation. This accounts for the observed  $P$ - $H$  loops with increased contribution from symmetric component, as  
 407 shown in Fig. S5.

408 Connection between the  $P$ - $M$  coupling and the  $H_C^{\text{ME}}(E)$  field is discussed in Fig. 14(a). The  $\tau=+1$  and  $\tau=-1$  states  
 409 can be also described in terms of  $\varphi^{\text{S}}$  as  $\varphi^{\text{S}} > 0$  and  $\varphi^{\text{S}} < 0$ , respectively, shown in Fig. 1(b). In the absence of external  
 410 fields, the two magnetoelectric states has the same free energy and they are separated by an energy barrier. In the  
 411 presence of  $H$ -field ( $H > H_C^{\text{ME}}(E)$ ) shown in Fig. 14(a), the energy barrier is reduced, and one of the magnetoelectric  
 412 state is selected according to the sign of the  $E$  and  $H$  fields (poling process). In this sense, the  $H_C^{\text{ME}}(E)$  is related to

413 the energy barrier separating the  $\tau=+1$  and  $\tau=-1$  states and considered to be an appropriate measure for the  $P$ - $M$   
414 coupling.

415 In order to understand the mechanism of the switching of  $P$ - $M$  clamping, we discuss the role of domain walls.  
416 When the external  $E$  or  $H$  field is reversed, the new majority domains expand, and  $P$ - or  $M$ -domain walls propagate  
417 throughout the sample. In the absence of  $P$ - $M$  coupling, these domain walls are independent and propagate  
418 separately. The  $P$ - $M$  coupling governs the possible types of the domain walls, and in the limit of strong coupling,  
419 only combined multiferroic domain walls are allowed<sup>44</sup>. In the present Y-type hexaferrites, the multiferroic domain  
420 walls are considered to be composed of simultaneously rotating  $P$  and  $M$  around the  $c$  axis while keeping their relative  
421 configuration unchanged<sup>28,29</sup>. However, when the combined domain walls with moderate coupling propagate through  
422 pinning centers or defects, the  $P$ - and  $M$ -domain walls may get deconfined from each other, and one of the two  
423 magnetoelectric states can be converted into another. This situation is microscopically different from, yet bears some  
424 resemblance with the simultaneous application of  $E$  and  $H$  fields. At low temperature, the spin canting angles  $\varphi^S$  and  
425  $\varphi^L$ , and hence the energy barrier between the  $\tau=+1$  and  $\tau=-1$  states is large [Fig. 14(b)], and the switching between  
426 them cannot occur. The  $P$ - and  $M$ -domain walls are confined, and the magnetoelectric response is anti-symmetric, as  
427 observed in Fig. 5 and also schematically shown in Fig. 14(c). However at high temperatures,  $\varphi^S$  and  $\varphi^L$ , and hence  
428 the energy barrier separating the two states becomes small and can be overcome by the increased thermal agitation.  
429 In this case the  $P$ - and  $M$ -domain walls are deconfined, making the magnetoelectric effect symmetric, as shown in  
430 Figs. S5 and 14(d).

## 431 V. SUMMARY

432 We have investigated the systematic change in the stability of several competing magnetic phases in the Y-type  
433 hexaferrites  $\text{Ba}_{2-y}\text{Sr}_y\text{Co}_2\text{Fe}_{12-x}\text{Al}_x\text{O}_{22}$  ( $x=0.9$ ) by changing the Ba/Sr ratio from  $y=0.8$  to  $y=1.2$ . The  $H$ - $T$  phase  
434 diagram that depends on the field history was studied by using magnetization, electric polarization, and neutron  
435 diffraction measurements for single crystal samples grown by laser floating zone method (see Figs. 1-5, and Sec. III D).  
436 The resistive properties of the synthesized crystals were much improved by the application of oxygen annealing  
437 procedure to allow the polarization measurements at high temperatures up to room temperature.

438 As a generic feature, these materials host the non-polar alternating longitudinal conical (ALC) and proper-screw  
439 (PS) phases in their zero-field-cooled state (see Fig. 1). Upon applying  $H$ -field perpendicular to the  $c$  axis ( $H_{\perp c}$ ),  
440 a multiferroic phase endowed with magnetoelectric functions, termed FE3 phase emerges. In our study, we found  
441 that the stability of the FE3 phase is improved as the Sr-doping level is increased (shown in Fig. 4). In the Ba-rich  
442 compound ( $y=0.8$ ), the FE3 phase is unstable and turns into the ALC phase when the  $H_{\perp c}$  field is removed at room  
443 temperature. In the compound with equal amount of Ba and Sr ( $y=1.0$ ), the FE3 phase is partially preserved in  
444 the absence of  $H_{\perp c}$  field after once applied. The FE3 phase is found to be most stable in the Sr-rich compound  
445 ( $y=1.2$ ) among the three compounds investigated in this study. It appears with other co-existing phases in the zero-  
446 field-cooled state but fully preserved below  $T=280$  K when the  $H_{\perp c}$  field is applied and even after  $H_{\perp c}$  is removed.  
447 It appears that the stability of the FE3 phase and interplay between the FE3 and ALC phases are influenced by a  
448 third magnetic phase, termed FE2' phase. The FE2' phase may be regarded as an intermediate state, which likely  
449 promotes the conversion between the FE3 and ALC magnetic orders. We discussed these findings in Sec. III D by  
450 using schematic illustrations for possible free energy diagrams. We note that the free energy diagrams are introduced  
451 phenomenologically, based on the magnetization and neutron diffraction data and not on actual calculations.

452 For the successful reversal of  $M$  by  $E$ -field, the existence of a stable multiferroic phase is necessary, but not  
453 sufficient. In some materials with symmetric magnetoelectric responses, the  $M$  does not change sign upon the  
454 reversal of  $E$ -field, and instead the magnetoelectric state is switched (see Figs. 7 and 8). This means that the free  
455 energy barrier separating the different states of the magnetoelectric phase has to be sufficiently large, in addition to  
456 those between the multiferroic phase and the non-polar magnetic phases. We addressed to these issues by selectively  
457 changing the electric and magnetic state with the application of large  $E$  and  $H$  fields for the samples in both multi-  
458 and single-domain magnetoelectric states. We found that the formation of the ALC phase is greatly suppressed in  
459 the single-domain magnetoelectric samples, which points to the importance of domain boundaries or walls in the  
460 phase conversion mechanism in these materials (see Fig. 9). The  $P$ - $M$  coupling was also studied by measuring the  
461 temperature dependence of the coercive fields, across which the two magnetoelectric states of the FE3 phase are  
462 switched to one another (shown in Figs. 10-14, and Sec. IV C).

463 Magnetization switching by  $E$ -field in the Y-type hexaferrites is realized by the propagation of complex  $P$ - and  
464  $M$ -domain walls with some mutual coupling<sup>29</sup>. When the canting angle of block-spin, and hence the energy barrier  
465 between the two magnetoelectric states of the FE3 phase is small, thermal agitation deconfines the  $P$ - and  $M$ -domain  
466 walls, leading to butterfly shaped  $M$  (see Fig. 14). Besides, when the energy barrier between the magnetoelectric and  
467 non-polar phases is small, the FE3 phase is turned into the ALC or PS phases, resulting in the complete loss of  $P$ - $M$

468 coupling. Therefore the double-fan structure of the FE3 phase have to be robust against thermal agitation and other  
 469 perturbations for the enhanced  $P$ - $M$  coupling. In order to keep the FE3 structure robust, strength of the exchange  
 470 interactions among the  $S^S$  and  $S^L$  spin-blocks have to be increased, while the anisotropy within the  $ab$  plane is further  
 471 reduced.

## 472 ACKNOWLEDGEMENTS

473 The authors are grateful for the fruitful discussion with Prof. Nicola Spaldin and Prof. Naoto Nagaosa. This  
 474 research used resources at the High Flux Isotope Reactor, a DOE Office of Science User Facility operated by the Oak  
 475 Ridge National Laboratory. This research was supported in part by the U.S.-Japan Cooperative Program on Neutron  
 476 Scattering. Structural unit cell of the Y-type hexaferrite crystal was illustrated using the software VESTA<sup>45</sup>.

- 
- 477 <sup>1</sup> T. Kimura, T. Goto, H. Shintani, K. Ishizaka, T. Arima, and Y. Tokura, *Nature* **426**, 55 (2003).  
 478 <sup>2</sup> N. Hur, P. A. Sharma, J. S. Ahn, S. Guha, and S.-W. Cheong, *Nature* **429**, 392 (2004).  
 479 <sup>3</sup> N. A. Spaldin and M. Fiebig, *Science* **309**, 391 (2005).  
 480 <sup>4</sup> T. Kimura, G. Lawes, and A. P. Ramirez, *Physical Review Letters* **94**, 137201 (2005).  
 481 <sup>5</sup> S. Ishiwata, Y. Taguchi, H. Murakawa, Y. Onose, and Y. Tokura, *Science* **319**, 1643 (2008).  
 482 <sup>6</sup> S. Fusil, V. Garcia, A. Barthélémy, and M. Bibes, *Annual Review of Materials Research* **44**, 91 (2014).  
 483 <sup>7</sup> D. Khomskii, *Physics* **2**, 20 (2009).  
 484 <sup>8</sup> H. Katsura, N. Nagaosa, and A. V. Balatsky, *Physical Review Letters* **95**, 057205 (2005).  
 485 <sup>9</sup> C. Jia, S. Onoda, N. Nagaosa, and J. H. Han, *Physical Review B* **74**, 224444 (2006).  
 486 <sup>10</sup> C. Jia, S. Onoda, N. Nagaosa, and J. H. Han, *Physical Review B* **76**, 144424 (2007).  
 487 <sup>11</sup> J. Wang, J. B. Neaton, H. Zheng, V. Nagarajan, S. B. Ogale, B. Liu, D. Viehland, V. Vaithyanathan, D. G. Schlom, U. V.  
 488 Waghmare, N. A. Spaldin, K. M. Rabe, M. Wuttig, and R. Ramesh, *Science* **299**, 1719 (2003).  
 489 <sup>12</sup> J. T. Heron, J. L. Bosse, Q. He, Y. Gao, M. Trassin, L. Ye, J. D. Clarkson, C. Wang, J. Liu, S. Salahuddin, D. C. Ralph,  
 490 D. G. Schlom, J. Iniguez, B. D. Huey, and R. Ramesh, *Nature* **516**, 370 (2014).  
 491 <sup>13</sup> M. Tokunaga, M. Akaki, T. Ito, S. Miyahara, A. Miyake, H. Kuwahara, and N. Furukawa, *Nature Communications* **6**, 5878  
 492 (2015).  
 493 <sup>14</sup> Y. Kitagawa, Y. Hiraoka, T. Honda, T. Ishikura, H. Nakamura, and T. Kimura, *Nat Mater* **9**, 797 (2010).  
 494 <sup>15</sup> S. H. Chun, Y. S. Chai, Y. S. Oh, D. Jaiswal-Nagar, S. Y. Haam, I. Kim, B. Lee, D. H. Nam, K.-T. Ko, J.-H. Park, J.-H.  
 495 Chung, and K. H. Kim, *Physical Review Letters* **104**, 037204 (2010).  
 496 <sup>16</sup> T. Kimura, *Annu. Rev. Condens. Matter Phys.* **3**, 93 (2012).  
 497 <sup>17</sup> V. Kocsis, Y. Tokunaga, S. Bordács, M. Kriener, A. Puri, U. Zeitler, Y. Taguchi, Y. Tokura, and I. Kézsmárki, *Phys. Rev.*  
 498 *B* **93**, 014444 (2016).  
 499 <sup>18</sup> Y. S. Chai, S. H. Chun, J. Z. Cong, and K. H. Kim, *Phys. Rev. B* **98**, 104416 (2018).  
 500 <sup>19</sup> H. Ueda, Y. Tanaka, Y. Wakabayashi, and T. Kimura, *Phys. Rev. B* **100**, 094444 (2019).  
 501 <sup>20</sup> Y. S. Chai, S. Kwon, S. H. Chun, I. Kim, B.-G. Jeon, K. H. Kim, and S. Lee, *Nat Commun* **5**, 4208 (2014).  
 502 <sup>21</sup> K. Zhai, Y. Wu, S. Shen, W. Tian, H. Cao, Y. Chai, B. C. Chakoumakos, D. Shang, L. Yan, F. Wang, and Y. Sun, *Nature*  
 503 *Communications* **8**, 519 (2017).  
 504 <sup>22</sup> K. Zhai, Y. Chai, J. Cong, D. Shang, and Y. Sun, *Phys. Rev. B* **98**, 144405 (2018).  
 505 <sup>23</sup> S. Ishiwata, Y. Taguchi, Y. Tokunaga, H. Murakawa, Y. Onose, and Y. Tokura, *Phys. Rev. B* **79**, 180408(R) (2009).  
 506 <sup>24</sup> Y. Hiraoka, H. Nakamura, M. Soda, Y. Wakabayashi, and T. Kimura, *Journal of Applied Physics* **110**, 033920 (2011),  
 507 <http://dx.doi.org/10.1063/1.3622332>.  
 508 <sup>25</sup> H. B. Lee, Y.-S. Song, J.-H. Chung, S. H. Chun, Y. S. Chai, K. H. Kim, M. Reehuis, K. Prokeš, and S. Mat'áš, *Phys. Rev.*  
 509 *B* **83**, 144425 (2011).  
 510 <sup>26</sup> H. Chang, H. B. Lee, Y.-S. Song, J.-H. Chung, S. A. Kim, I. H. Oh, M. Reehuis, and J. Schefer, *Phys. Rev. B* **85**, 064402  
 511 (2012).  
 512 <sup>27</sup> S. Hirose, K. Haruki, A. Ando, and T. Kimura, *Applied Physics Letters* **104**, 022907 (2014).  
 513 <sup>28</sup> T. Nakajima, Y. Tokunaga, M. Matsuda, S. Dissanayake, J. Fernandez-Baca, K. Kakurai, Y. Taguchi, Y. Tokura, and T.-h.  
 514 Arima, *Phys. Rev. B* **94**, 195154 (2016).  
 515 <sup>29</sup> V. Kocsis, T. Nakajima, M. Matsuda, A. Kikkawa, Y. Kaneko, J. Takashima, K. Kakurai, T. Arima, F. Kagawa, Y. Tokunaga,  
 516 Y. Tokura, and Y. Taguchi, *Nature Communications* **10**, 1247 (2019).  
 517 <sup>30</sup> Y. Kaneko and Y. Tokura, *Journal of Crystal Growth* **533**, 125435 (2020).  
 518 <sup>31</sup> Y. Inaguma, T. Katsumata, R. Wang, K. Kobashi, M. Itoh, Y.-J. Shan, and T. Nakamura, *Ferroelectrics* **264**, 127 (2001),  
 519 <https://doi.org/10.1080/00150190108008558>.  
 520 <sup>32</sup> J. Smit and H. P. J. Wijn, *Ferrites* (Philips Research Laboratories, 1959).  
 521 <sup>33</sup> N. Momozawa, Y. Yamaguchi, H. Takei, and M. Mita, *Journal of the Physical Society of Japan* **54**, 771 (1985).

- 522 <sup>34</sup> N. Momozawa and Y. Yamaguchi, *Journal of the Physical Society of Japan* **62**, 1292 (1993),  
523 <http://dx.doi.org/10.1143/JPSJ.62.1292>.
- 524 <sup>35</sup> S. Utsumi, D. Yoshiba, and N. Momozawa, *Journal of the Physical Society of Japan* **76**, 034704 (2007).
- 525 <sup>36</sup> S. Ishiwata, D. Okuyama, K. Kakurai, M. Nishi, Y. Taguchi, and Y. Tokura, *Phys. Rev. B* **81**, 174418 (2010).
- 526 <sup>37</sup> H. B. Lee, Y.-S. Song, J.-H. Chung, S. H. Chun, Y. S. Chai, K. H. Kim, M. Reehuis, K. Prokeš, and S. Mat'áš, *Phys. Rev.*  
527 *B* **83**, 144425 (2011).
- 528 <sup>38</sup> See Supplemental Material at [URL will be inserted by the production group] for further magnetization, polarization, and  
529 neutron diffraction measurements.
- 530 <sup>39</sup> M. Mostovoy, *Physical Review Letters* **96**, 067601 (2006).
- 531 <sup>40</sup> I. A. Sergienko and E. Dagotto, *Physical Review B* **73**, 094434 (2006).
- 532 <sup>41</sup> E. Hassanpour, M. C. Weber, A. Bortis, Y. Tokunaga, Y. Taguchi, Y. Tokura, A. Cano, T. Lottermoser, and M. Fiebig,  
533 “Interconversion of multiferroic domains and domain walls,” (2019), [arXiv:1908.06876 \[cond-mat.mtrl-sci\]](https://arxiv.org/abs/1908.06876).
- 534 <sup>42</sup> K. Kimura, H. Nakamura, S. Kimura, M. Hagiwara, and T. Kimura, *Physical Review Letters* **103**, 107201 (2009).
- 535 <sup>43</sup> Y. Tokunaga, Y. Taguchi, T. Arima, and Y. Tokura, *Physical Review Letters* **112**, 037203 (2014).
- 536 <sup>44</sup> Y. Tokunaga, N. Furukawa, H. Sakai, Y. Taguchi, T.-h. Arima, and Y. Tokura, *Nat Mater* **8**, 558 (2009).
- 537 <sup>45</sup> K. Momma and F. Izumi, *Journal of Applied Crystallography* **41**, 653 (2008).

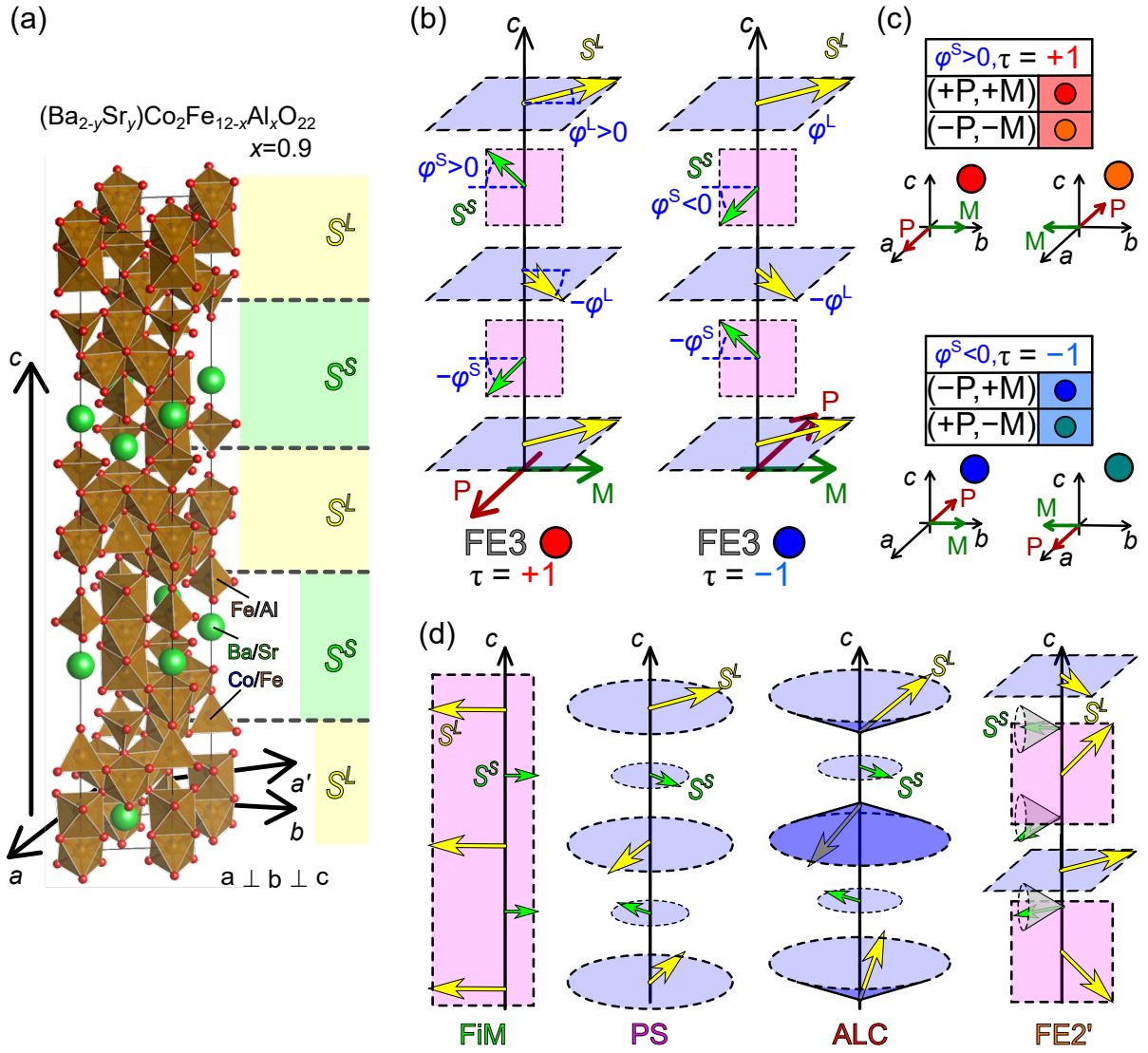


FIG. 1. (Color online) (a) The hexagonal unit cell of the Y-type hexaferrite  $\text{Ba}_{2-y}\text{Sr}_y\text{Co}_2\text{Fe}_{12-x}\text{Al}_x\text{O}_{22}$  ( $x=0.9$ ), shown together with alternating layers of the  $S^L$  and  $S^S$  spin-blocks. While the  $a$ ,  $a'$ , and  $c$  lattice vectors span the hexagonal basis, we define the orthogonal axis  $b$  ( $\propto c \times a$ ) for the convenient description of the experiments. (b) The block-spins in the FE3 phase form a double-fan structure, where the  $S^L$  and  $S^S$  are confined within the orthogonal  $ab$  and  $ac$  planes, respectively. The spin-driven  $\mathbf{P}$  is induced perpendicular to the net  $\mathbf{M}$ , which can rotate around the  $c$  axis almost freely due to the negligible anisotropy within the  $ab$  plane. The  $S^L$  and  $S^S$  block-spins are specified by the angles  $\varphi^L$  and  $\varphi^S$ , respectively, as indicated in the right panel. The phase between the  $S^L$  and  $S^S$  spin-blocks is different in the two independent magnetoelectric states of the FE3 phase, labeled as  $\tau = +1$  and  $\tau = -1$ .  $\varphi^L > 0$  is assumed without losing generality, and then the  $\tau = +1$  magnetoelectric state has  $\varphi^S > 0$ , while the  $\tau = -1$  state has  $\varphi^S < 0$ . (c) The four independent  $(\pm P, \pm M)$  states of the FE3 phase with  $\mathbf{P} \perp \mathbf{M}$ ;  $\mathbf{P}, \mathbf{M} \perp c$  are classified according to the  $P$ - $M$  coupling. The  $(+P, +M)$  and  $(-P, -M)$  states are essentially the same states and are categorized as the  $\tau = +1$  magnetoelectric state. On the other hand,  $(-P, +M)$  and  $(+P, -M)$  states are classified together to form the  $\tau = -1$  state. The magnetoelectric state is selected by the application of high electric ( $E$ ) and magnetic ( $H$ ) fields in the  $\mathbf{E} \perp \mathbf{H}$ ;  $\mathbf{E}, \mathbf{H} \perp c$  configuration. (d) Schematic illustration of the collinear ferrimagnetic (FiM), proper screw (PS), alternating longitudinal conical (ALC) and the FE2' phases. Note that only the illustration for the FE2' phase is compressed along the  $c$  axis.

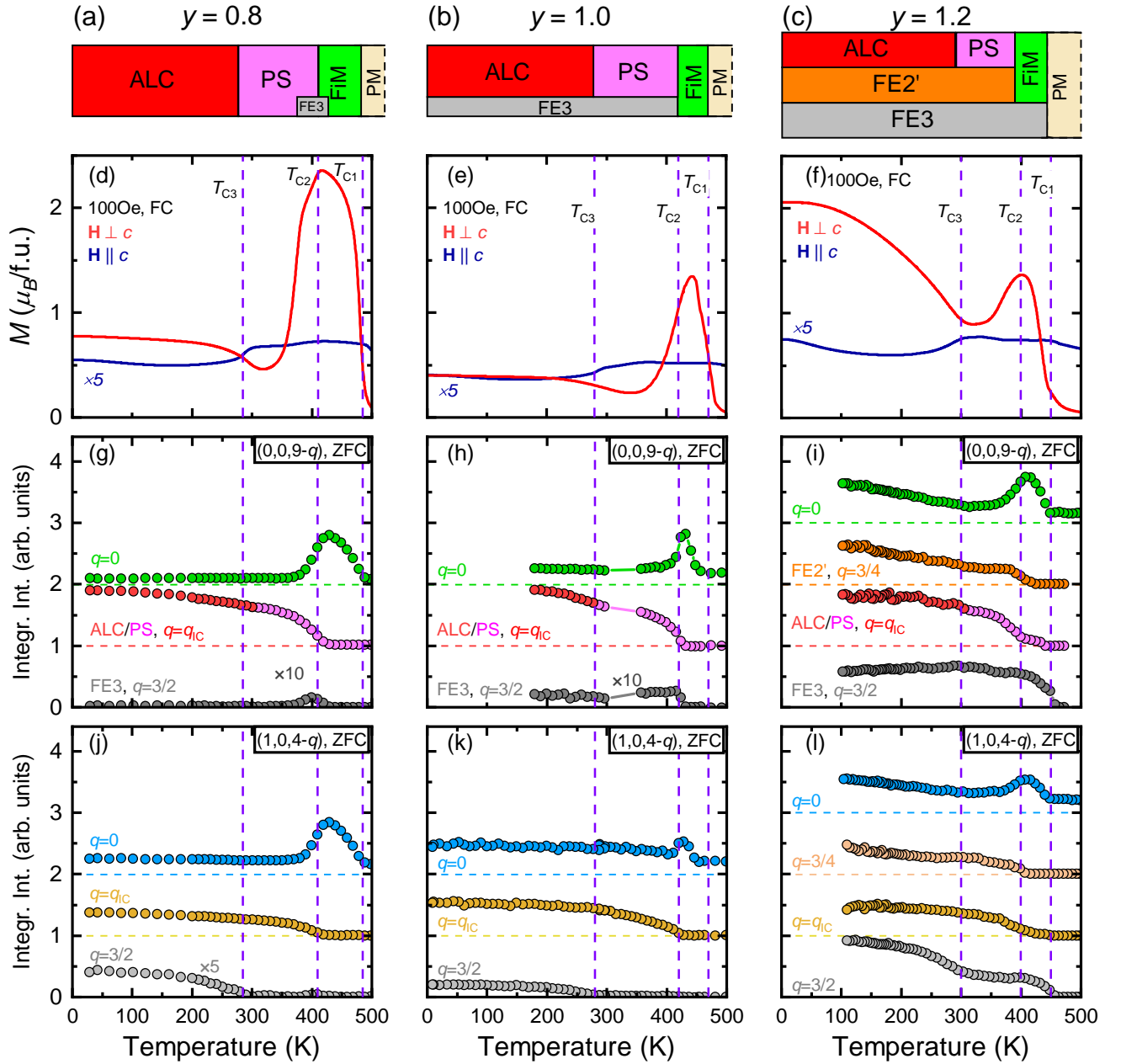


FIG. 2. (Color online) (a-c) Magnetic phase diagrams of  $\text{Ba}_{2-y}\text{Sr}_y\text{Co}_2\text{Fe}_{12-x}\text{Al}_x\text{O}_{22}$  ( $x=0.9$ ) with different Ba/Sr ratios, (a)  $y=0.8$ , (b)  $y=1.0$ , and (c)  $y=1.2$  in the zero-field-cooled (ZFC) state. The magnetic structures for respective phases are illustrated in Fig. 1. (d-f) Temperature dependence of the low-field-cooled (FC) magnetization  $M_{\perp c}$  and  $M_{\parallel c}$  for  $\mathbf{H} \perp c$  and  $\mathbf{H} \parallel c$ , respectively, measured in 100 Oe field. Note that the  $M_{\parallel c}$  is multiplied by 5 for better visibility. (g-l) Integrated intensities of the neutron diffraction peaks for  $q=0$ ,  $3/4$ ,  $3/2$ , and  $q_{IC}$  measured in the ZFC runs. The scattering intensities were measured along the  $(0,0,9-q)$  and  $(1,0,4-q)$  lines, respectively for the data shown in panels (g-i) and panels (j-l).

541

542

543

544

545

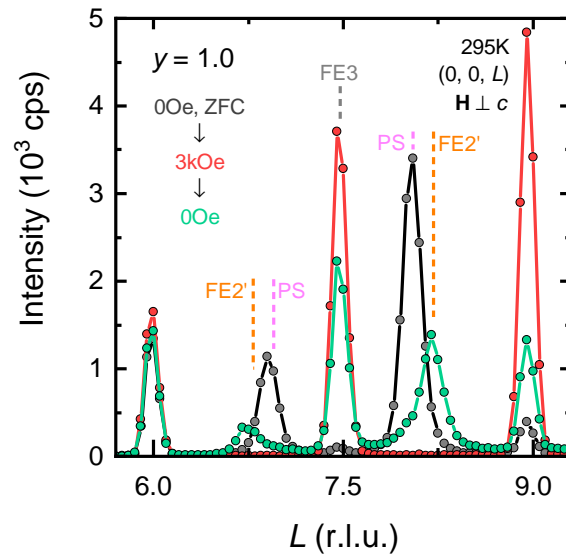


FIG. 3. (Color online) Neutron diffraction profiles of the  $y=1.0$  compound measured at  $T=295$  K after ZFC, in the presence of  $H=3$  kOe applied perpendicular to the  $c$  axis, and after the removal of the  $H$  field. Vertical dashed lines indicate the  $q_{1C}$  (of the PS phase), the  $q=3/2$  (of the FE3 phase), and the  $q=3/4$  (of the FE2' phase) modulation vectors.

546

547

548

549

550



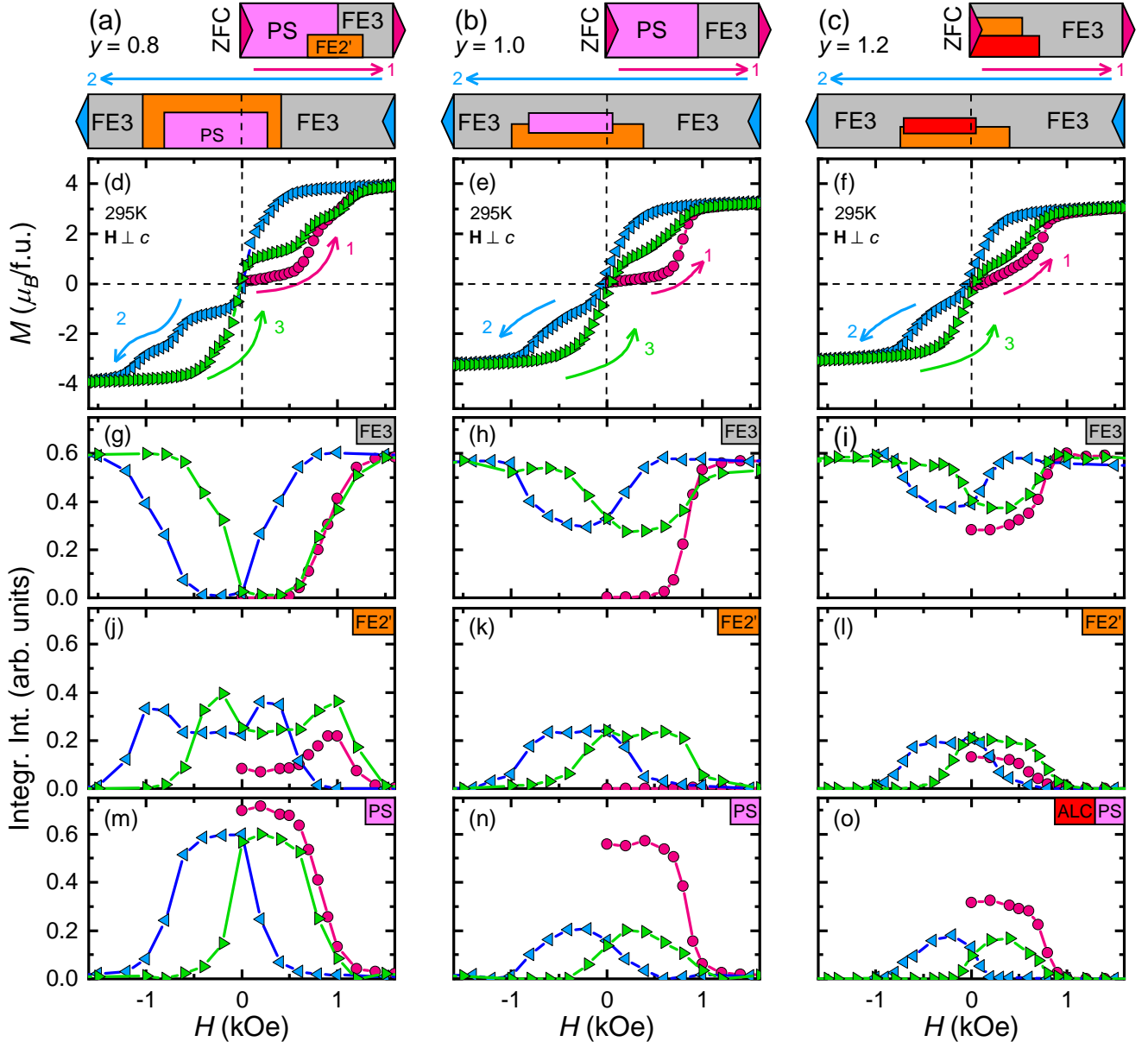


FIG. 4. (Color online) (a-c) Field-history dependent magnetic phase diagrams of the  $Ba_{2-y}Sr_yCo_2Fe_{12-x}Al_xO_{22}$  ( $x=0.9$ ) hexaferrite compounds in  $\mathbf{H} \perp c$  field at  $T=295$  K. The red circular symbols (1) in panels (d-o) denote the initial curves measured after the **zero-field-cooling (ZFC)** and corresponds to the first line of the phase diagrams (a-c). The blue left-triangular symbols (2) indicate the field-decreasing runs and are related to the second line of the  $H \perp c$  phase diagrams in panels (a-c). The green right-triangular symbols (3) represent the data collected in the field-increasing runs. (d-f)  $M-H_{\perp c}$  measured at  $T=295$  K. (g-o) Magnetic-field dependence of the integrated intensities of selected magnetic reflections related to the FE3, the FE2', and the incommensurate PS/ALC phases. The phases are represented by the  $q=3/2$ ,  $3/4$ , and  $q_{1C}$  reflections measured along the  $(0,0,L)$  line, respectively. Data for the  $y=1.2$  compound are reproduced from Ref. 29

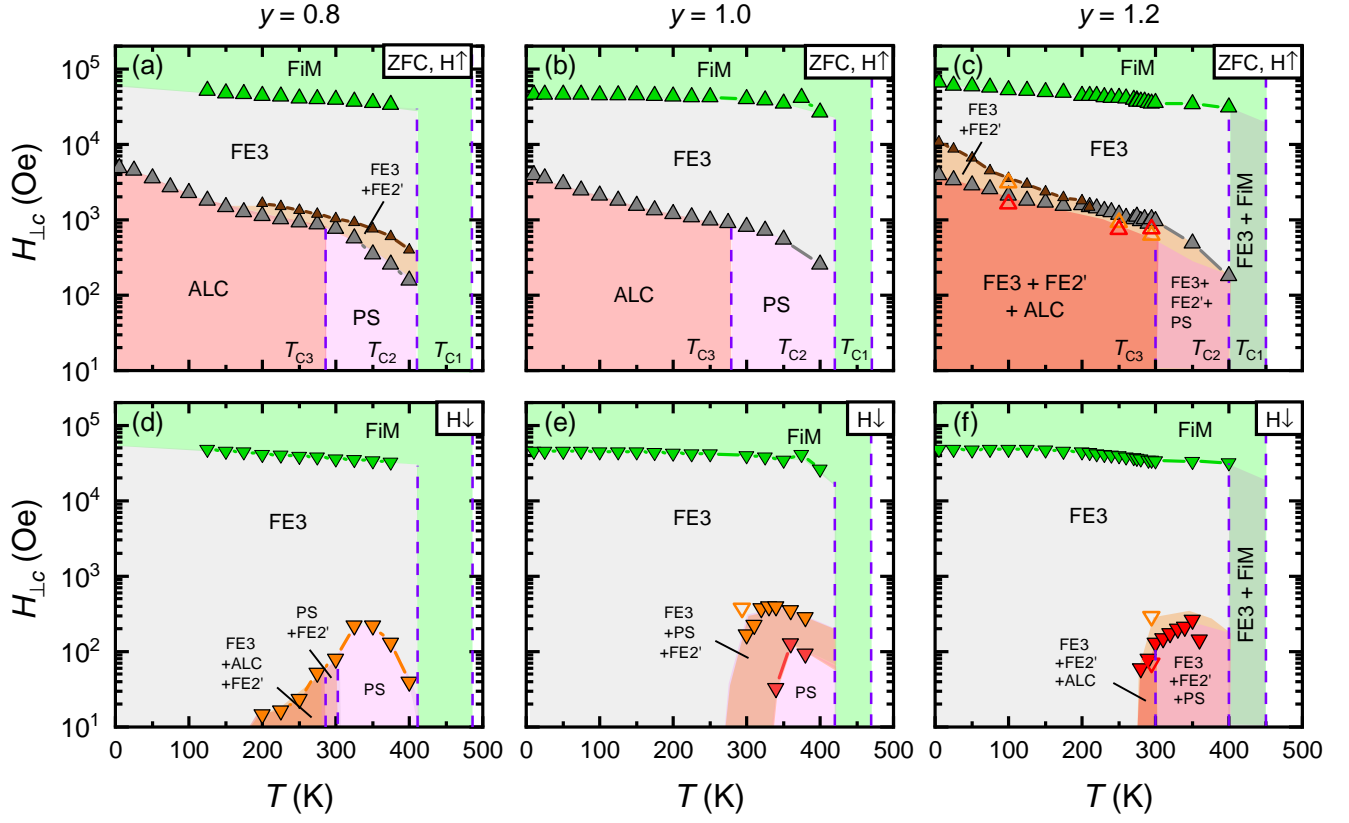


FIG. 5. (Color online) The magnetic phase diagrams of the Y-type hexaferrites  $\text{Ba}_{2-y}\text{Sr}_y\text{Co}_2\text{Fe}_{12-x}\text{Al}_x\text{O}_{22}$  ( $x=0.9$ ) with different Ba/Sr ratios for  $\mathbf{H} \perp c$  configuration. Panels (a,d), (b,e), and (c,f) correspond to the samples with  $y=0.8$ , 1.0, and 1.2, respectively. Panels (a-c) show the phase diagrams in the field-increasing runs after ZFC (upward triangles), while panels (d-f) are those in the field-decreasing experiments (downward triangles). The phase boundaries are determined as the anomalies in the  $M$ - $H$  curves (closed symbols), while the identification of the phases is based on the neutron diffraction measurements (open symbols).

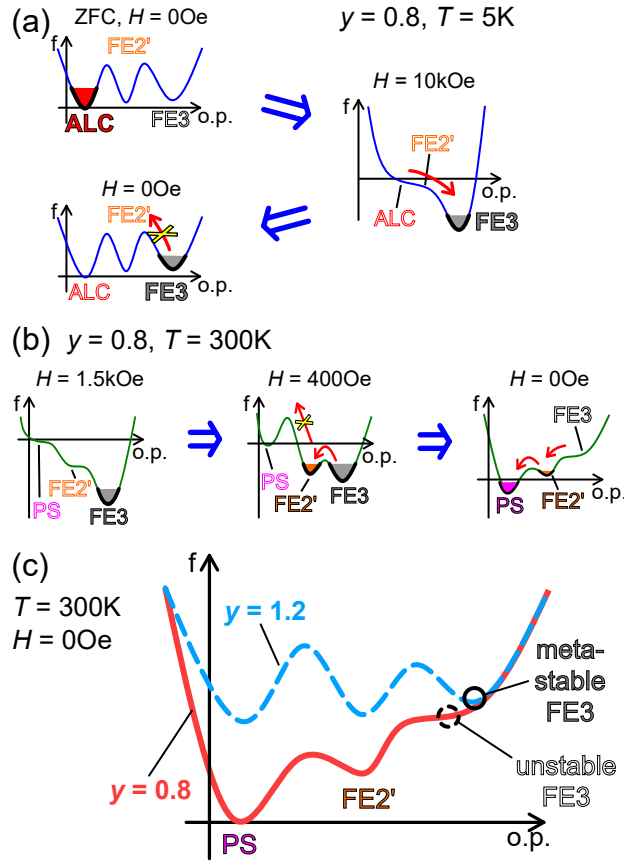


FIG. 6. (Color online) (a) Metastability of the multiferroic FE3 phase exemplified for the  $y=0.8$  compound at low temperature. The **alternating longitudinal conical (ALC)** phase has the lowest free energy in the phase space of the order parameter (simplified as o.p. axis), therefore the ALC is stabilized by the **zero-field-cooling (ZFC)** process as an initial state. Application of  $H_{\perp c}$  field lowers the free energy of the FE3 phase, which is stabilized and preserved when the field is removed. The FE3 phase is separated from the ALC phase by a large energy barrier and robust against thermal fluctuations. At this temperature the FE2' phase has minor impact. (b) Schematic illustration of the free energy landscape for  $y=0.8$  compound at specific values of the  $H_{\perp c}$  in the field decreasing run at 300 K. In the presence of high  $H_{\perp c}$  field of 1.5 kOe, the FE3 phase is stable. At lower fields, the energy barrier between the FE3 and FE2' phase decreases, while the barrier to the PS phase is still significant. In the absence of  $H_{\perp c}$  field, the FE3 phase is unstable and disappears, while the PS phase emerges. (c) Schematic illustration of the free energy landscape for the  $y=0.8$  and 1.2 compounds. In the  $y=0.8$  compound, the free energy barrier between the FE3 and PS phases is more reduced than in the  $y=1.2$  due to the presence of the FE2' phase.

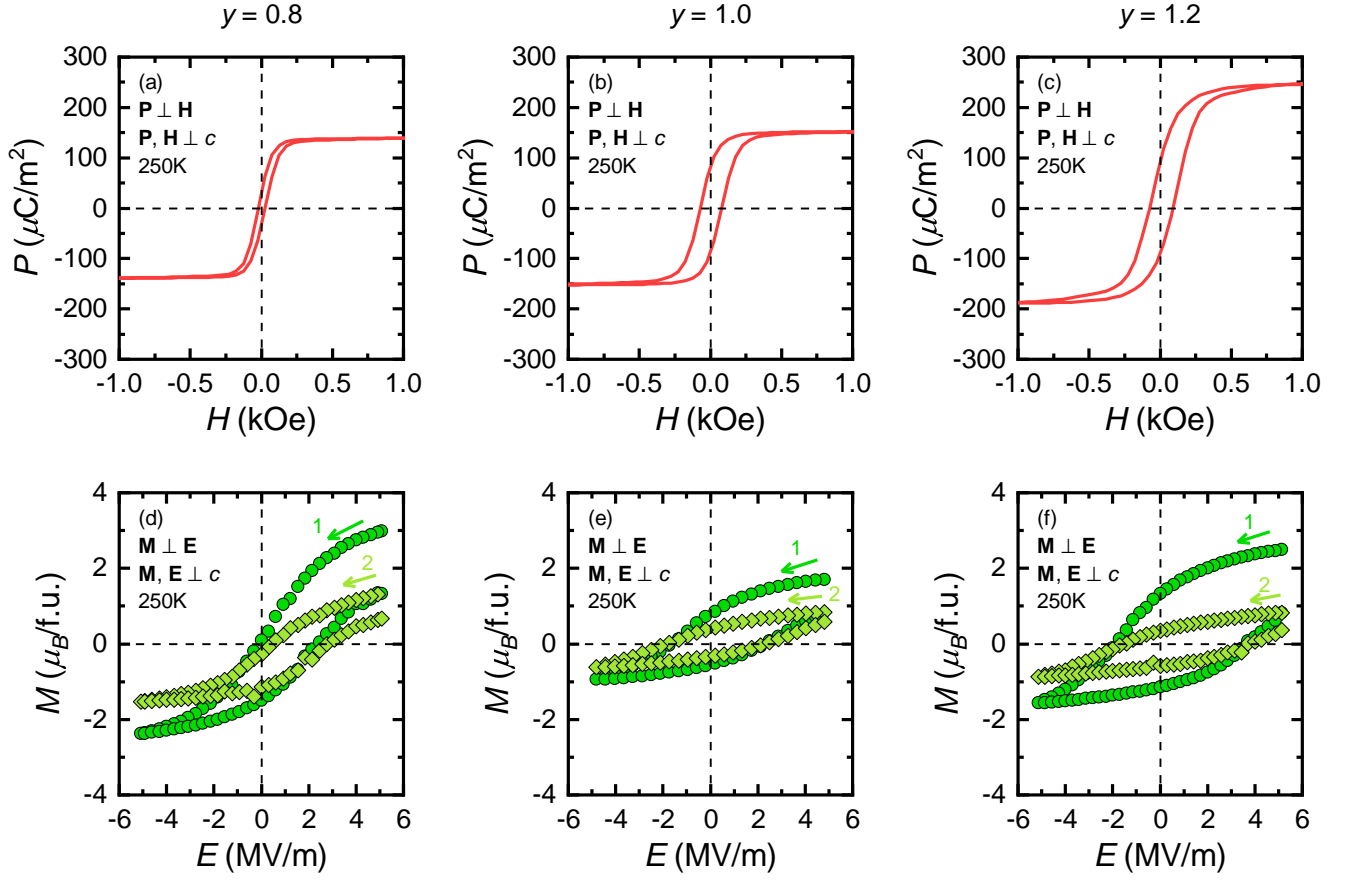


FIG. 7. (Color online) The magnetolectric responses in  $\text{Ba}_{2-y}\text{Sr}_y\text{Co}_2\text{Fe}_{12-x}\text{Al}_x\text{O}_{22}$  ( $x=0.9$ ) are demonstrated. In (a-c) and (d-f),  $P$ - $H$  and  $M$ - $E$  curves at 250 K are presented. Both the  $P$ - $H$  and  $M$ - $E$  curves exhibit anti-symmetric field dependence at this temperature. Panels (a,d), (b,e), and (c,f) correspond to the compounds with  $y=0.8$ , 1.0, and 1.2, respectively.

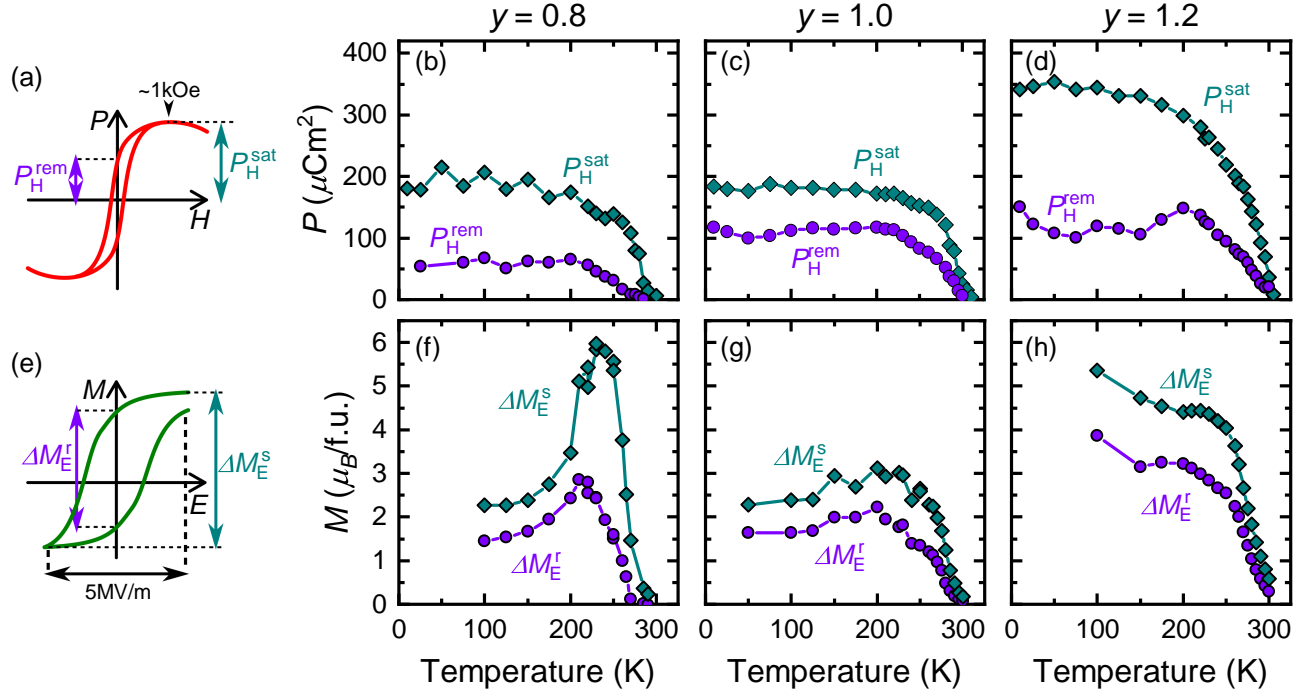


FIG. 8. (Color online) (a) Schematic illustration of a  $P$ - $H$  loop showing the definition for the saturation ( $P_H^{\text{sat}}$ ) and remanent ( $P_H^{\text{rem}}$ ) values of the polarization of magnetic origin. (b-d) Temperature dependence of  $P_H^{\text{sat}}$  and  $P_H^{\text{rem}}$  in the Ba<sub>2-y</sub>Sr<sub>y</sub>Co<sub>2</sub>Fe<sub>12-x</sub>Al<sub>x</sub>O<sub>22</sub> ( $x=0.9$ ) with  $y=0.8$ , 1.0, and 1.2 in panels (b), (c), and (d), respectively. Note that panels (b-d) share common scales for the vertical axis while the horizontal axes are the same with (f)-(h). (e) Schematic illustration of an  $M$ - $E$  curve. The  $\Delta M_E^s$  is defined as the magnetization change between  $E=\pm 5\text{MV}/\text{m}$  fields, while  $\Delta M_E^r$  is the change in the remanent magnetization for the first cycle of the  $E$  field. (f-h) Temperature dependence of the  $\Delta M_E^s$  and  $\Delta M_E^r$  in all the three compounds shown with common scale for the vertical axis.

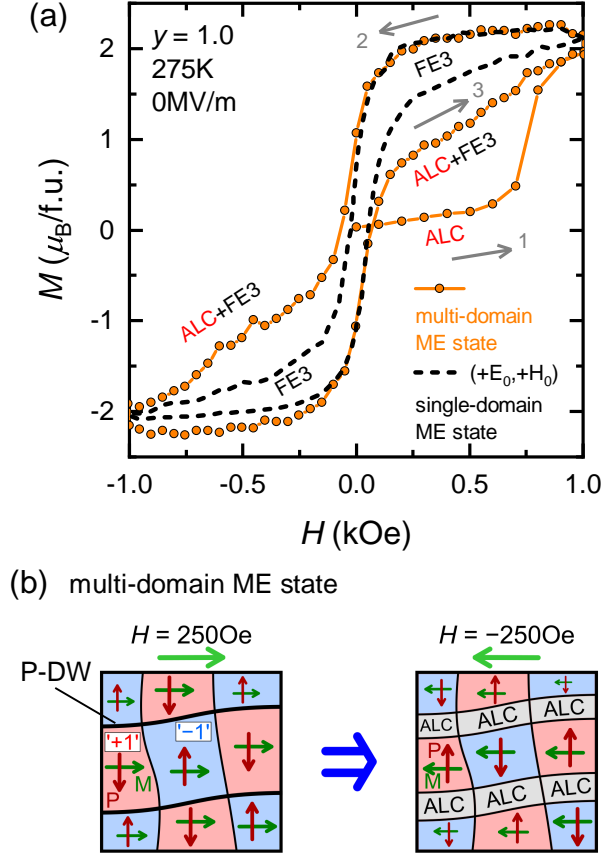


FIG. 9. (Color online) (a) Magnetization curves of the  $y=1.0$  sample in multi- and single-domain **magnetolectric (ME)** states taken in the absence of  $E$ -field. Without magnetolectric poling, the ALC phase reappears just after the sign reversal of the  $H$  field (orange curve). In the single-ME-domain case, the FE3 phase is preserved throughout the experiment (black, dashed curve). The single-domain state was prepared by applying  $E_0=+5$  MV/m,  $H_0=+50$  kOe fields. (b) Schematic illustration of the multi-domain ME state within the  $ab$  plane upon the reversal of the in-plane  $H$  field. The red and blue regions correspond to the  $\tau=+1$  and  $\tau=-1$  ME states of the FE3 phase, respectively. **P-DW** denotes the **polarization domain walls**. The **alternating longitudinal conical (ALC)** phase is shown as grey area in the right panel. Green and red arrows indicate the direction of  $M$  and  $P$ , respectively. The ALC phase can form at the edges of the magnetolectric domains, where  $P$  can be zero to reduce the electrostatic energy originating from the head-to-head or tail-to-tail configuration. In the multi-domain case, the ALC phase can readily expand into macroscopic domains. In the single-domain state, the ALC phase is difficult to nucleate.

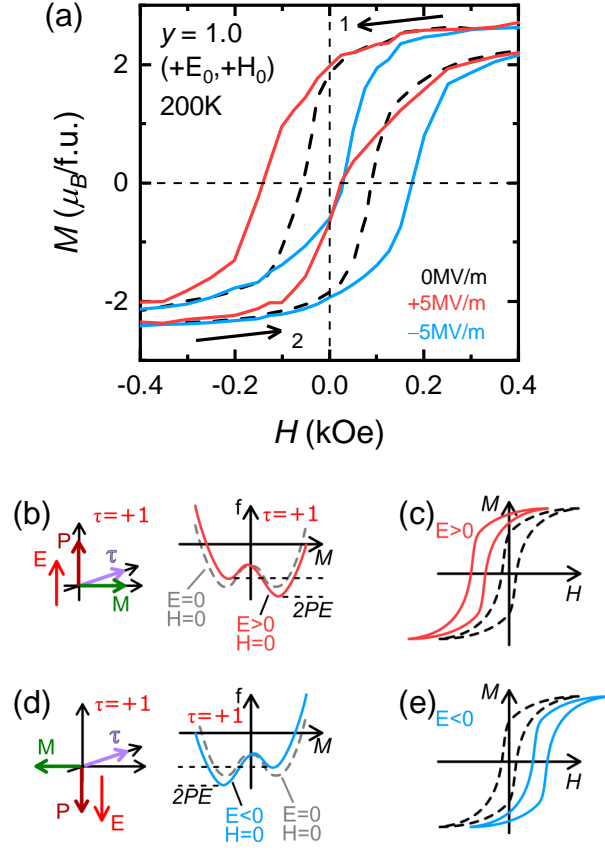


FIG. 10. (Color online) (a)  $E$ -field biased  $M$ - $H$  measurements on a sample with  $y=1.0$  in a single-domain magnetoelectric-state, prepared by  $E_0=+5$  MV/m,  $H_0=+50$  kOe poling fields at  $T=200$  K. (b-e) Schematic illustration of the  $E$ -field biased  $M$ - $H$  measurements on a sample in the  $\tau=+1$  magnetoelectric state. (b) In the presence of  $E > 0$  field, the free energy of the  $+P$ , and therefore the  $+M$  states are lowered. Hence, the  $+M$  state is more stable than the  $-M$  state even in the absence of  $H$  field. (c) As larger negative field is needed for the  $M$  switching to compensate the electrostatic energy, the  $M$ - $H$  hysteresis is shifted to the  $-H$  direction. (d) In the presence of  $E < 0$  field, the free energy of the state with  $-P$  and  $-M$  is lowered. (e) In this case the  $M$ - $H$  hysteresis is shifted towards the  $+H$  direction.

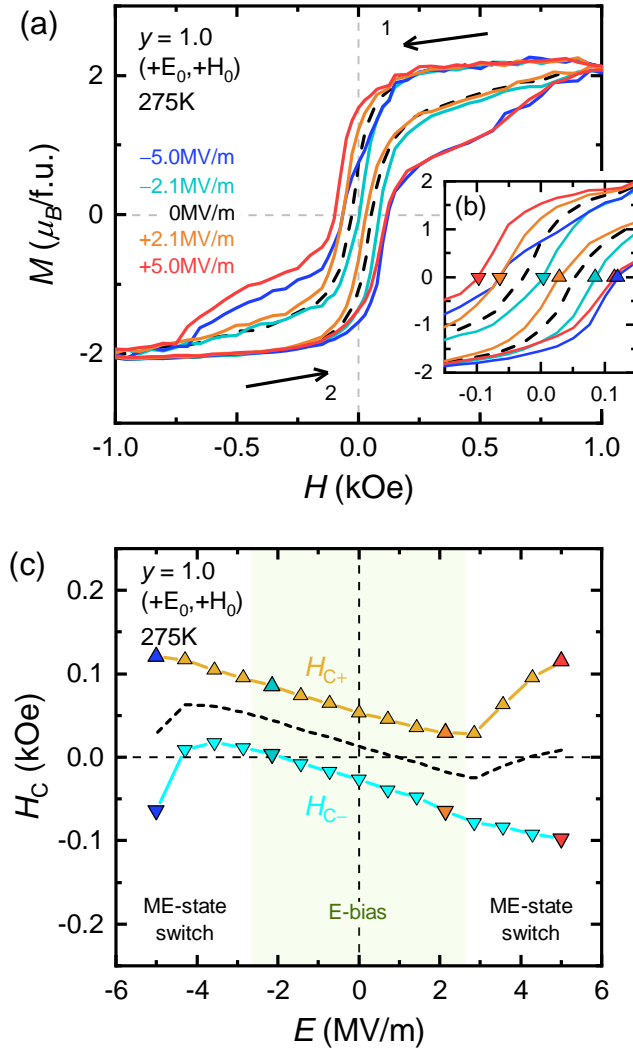


FIG. 11. (Color online) (a) Magnetization curves of the  $y=1.0$  sample at  $T=275$  K in the presence of several  $E$  fields. The measurement was started from the single-domain magnetoelectric-state, attained by  $E_0=+5$  MV/m,  $H_0=+50$  kOe poling fields. (b) Expanded view of the  $M-H$  loops of panel (a). The upward (downward) triangles indicate the  $H_{C+}$  ( $H_{C-}$ ) coercive fields in the field-increasing (decreasing) runs. (c) Electric field dependence of  $H_{C+}$  and  $H_{C-}$  coercive fields. Black dashed line indicates the average of  $H_{C+}$  and  $H_{C-}$ . For  $|E| < 3$  MV/m fields, the coercive fields show linear  $E$ -field dependence. For larger  $E$  fields,  $H_C$  deviates from the linear relation, indicating that the magnetoelectric state is switched. In addition, the ALC phase reappears during the field-sweeping (see panel (a)).



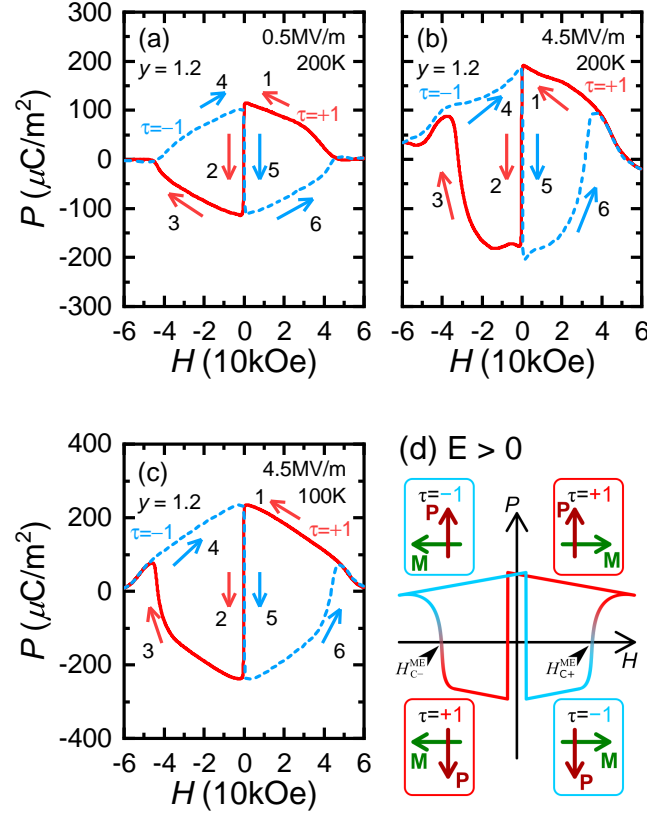


FIG. 12. (Color online) (a,b) Magnetic-field dependence of polarization ( $P$ - $H$ ) for  $y=1.2$  compound at  $T=200\text{ K}$  in the presence of  $E=0.5\text{ MV/m}$  and  $4.5\text{ MV/m}$  in panels (a) and (b), respectively. The numbered arrows indicate the sequence of the measurement, starting from the FiM phase at  $H=60\text{ kOe}$ . (c)  $P$ - $H$  loop measured in the presence of  $E=4.5\text{ MV/m}$  field at  $T=100\text{ K}$ . (d) Schematic illustration of a  $P$ - $H$  hysteresis loop in the presence of large  $E (> 0)$  field. Simultaneous application of large  $E$  and  $H$  fields switches the magnetoelectric state between the  $\tau=+1$  and  $\tau=-1$ . The coercive fields  $H_{C_{\pm}}^{\text{ME}}$  correspond to the  $H$  field needed to switch between the  $\tau=+1$  and  $\tau=-1$  states for a given value of the  $E$  field.

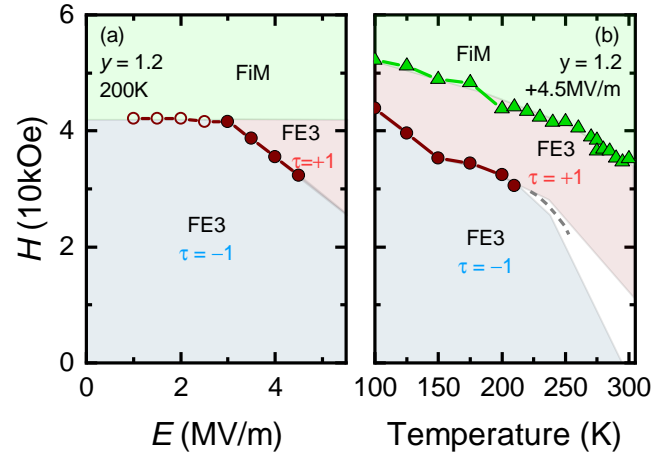


FIG. 13. (Color online) (a) The  $H$ - $E$  phase diagram for  $y=1.2$  compound at  $T=200\text{ K}$ , showing the  $\tau=-1$  and  $\tau=+1$  magnetoelectric states of the FE3 phase as well as the ferrimagnetic (FiM) phase. Data points are taken in the  $H$ -increasing run from  $-60\text{ kOe}$  to  $+60\text{ kOe}$  in the presence of positive  $E$ -fields. Open and full symbols correspond to partial and complete switching between the magnetoelectric states. The boundary separating the  $\tau=-1$  and  $\tau=+1$  states has strong  $E$ -dependence for the high-field region, while the FiM-FE3 phase boundary is independent of the  $E$  field. (b) The  $H$ - $T$  phase diagram showing the  $\tau=-1$  and  $\tau=+1$  states of the FE3 phase and the FiM phase in the presence of  $E=4.5\text{ MV/m}$  field determined in the  $H$ -increasing runs at each temperature. The boundary between the  $\tau=-1$  and  $\tau=+1$  states is the  $E$ -dependent coercive field  $H_C^{\text{ME}}$  needed to switch between the magnetoelectric states.

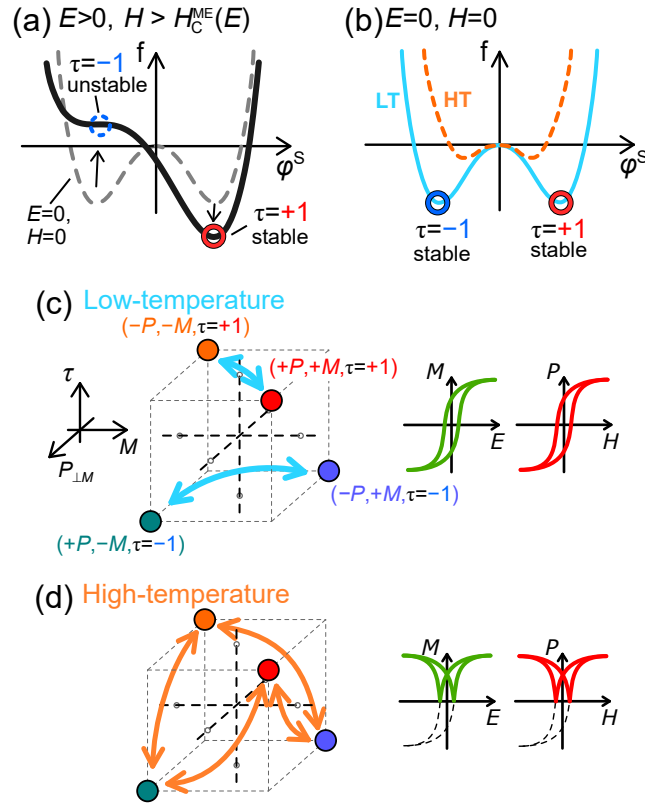


FIG. 14. (Color online) (a) Free energy of the FE3 phase as a function of the canting angle of the  $S^S$  block spin. In the absence of  $E$  and  $H$  fields, free energies for the  $\tau=+1$  and  $\tau=-1$  states are degenerate (dashed curve). When large  $E$  and  $H$  fields are applied ( $H > H_C^{\text{ME}}(E)$ ) simultaneously, the free energy barrier vanishes, and the  $\tau=+1$  state is stabilized, while the  $\tau=-1$  state is destabilized. (b) Schematic illustration of the free energy landscape showing the  $\tau=+1$  and  $\tau=-1$  states of the FE3 phase at low (LT) and high (HT) temperatures. The magnetic state is described by the  $\varphi^S$  angle and the states are separated by a free energy barrier. At low temperature, the energy barrier is large and the magnetoelectric states are robust. At high temperatures, the energy barrier is small and the magnetoelectric state can be switched easily. (c) Order parameter phase space spanned by  $P$ ,  $M$ , and  $\tau$  axes (left). At low temperatures, the  $P$ - $M$  coupling is strong, and once a magnetoelectric state is selected ( $\tau=+1$  or  $\tau=-1$ ) by the poling  $E$  and  $H$  fields, it is preserved. Then, the magnetoelectric response, *i.e.* the  $M$ - $E$  and  $P$ - $H$  curves show anti-symmetric field dependence (right). (d) At high temperatures, the  $P$ - $M$  coupling is weak and the initial states are not preserved. Hence, switching between  $\tau=+1$  and  $\tau=-1$  states occurs as indicated by orange arrows. The switching between the states results in the symmetric magnetoelectric response, *i.e.* symmetric  $M$ - $E$  and  $P$ - $H$  loops as shown in the right panel.